

MHD Models of Axisymmetric Protostellar Jets

James M. Stone

Department of Astronomy, University of Maryland, College Park, MD 20742
jstone@astro.umd.edu

Philip E. Hardee

Department of Physics & Astronomy, The University of Alabama, Tuscaloosa, AL 35487
hardee@athena.astr.ua.edu

Received _____; accepted _____

ABSTRACT

We present the results of a series of axisymmetric time-dependent magnetohydrodynamic (MHD) simulations of the propagation of cooling, overdense jets. Our numerical models are motivated by the properties of outflows associated with young stellar objects. A variety of initial field strengths and configurations are explored for both steady and time-variable (pulsed) jets. For the parameters of protostellar jets adopted here, even apparently weak magnetic fields with strengths $B \gtrsim 60\mu\text{G}$ in the pre-shocked jet beam can have a significant effect on the dynamics, for example by altering the density, width, and fragmentation of thin shells formed by cooling gas. Strong toroidal fields ($\geq 100\mu\text{G}$) with a radial profile that peaks near the surface of the jet result in the accumulation of dense shocked gas in a “nose cone” at the head of jet. We suggest that this structure is unstable in three-dimensions. A linear analysis predicts that axisymmetric pinch modes of the MHD Kelvin-Helmholtz instability should grow only slowly for the highly supermagnetosonic jets studied here; we find no evidence for them in our simulations. Some of our models appear unstable to current-driven pinch modes, however the resulting pressure and density variations induced in the jet beam are not large, making this mechanism an unlikely source of emission knots in the jet beam. In the case of pulsed jets, radial hoop stresses confine shocked jet material in the pulses to the axis, resulting in a higher density in the pulses in comparison to purely hydrodynamic models. In addition, if the magnetic field strength varies with radius, significant radial structure is produced in the pulses (the density is strongly axially peaked, for example) even if the density and velocity in the jet follow a constant “top-hat” profile initially.

Subject headings: hydrodynamics — magnetohydrodynamics — ISM: jets and outflows — galaxies: jets

1. Introduction

The most promising mechanism for the production of supersonic, highly collimated jets from low mass young stellar objects is by magnetic forces associated either directly with an accretion disk (Königl & Pudritz 1999), or with the interaction between an accretion disk and a magnetized central star (Shu et al. 1999). Magnetic fields are also thought to contribute to the collimation of the jets on larger scales, (although only slowly so that the observed jet may only be a part of a much broader wind, e.g., Ostriker 1997). Thus, unless the outflowing material is highly resistive (which seems unlikely), protostellar jets should contain a dynamically important magnetic field which may affect both the propagation and stability of the outflow. Observation of the magnetic field strength associated with protostellar jets is difficult. However, by fitting one-dimensional radiative shock models to the observed line ratios in the bow shock of HH47, Morse et al. (1993) inferred an upper limit to the magnetic field in the ambient medium upstream of the jet of $\sim 30\mu\text{G}$, a value which they argued was too small to affect the dynamics except by increasing the cooling lengths behind radiative shocks. More recently, Ray et al. (1997) have reported direct evidence for strong fields in the outflow associated with the source T Tau S through the detection of opposite circular polarization in the two spatially resolved outflow lobes. These authors infer very high field strengths within the lobes; several Gauss at a distance of few tens of AU from the central star.

If protostellar jets contain strong magnetic fields as expected from theory, there may be a signature of such fields in their dynamics. While hydrodynamical studies of cooling, dense protostellar jets are widely available in the literature (e.g., see Raga 1995; Cabrit 1997 for reviews), MHD models are less well explored. MHD studies of extragalactic (i.e., *underdense* and *non-radiative*) jets have been reported by Clarke, Norman, & Burns (1986), and Lind et al. (1989) for the case of toroidal fields, and by Kössl et al. (1990a; 1990b) for the case of toroidal and axial fields (see also Clarke 1996 for a recent review). For strong fields, characterized by a small value of $\beta \equiv 8\pi P/B^2$ where B is the field strength and P the thermal pressure (although note such fields may still have an energy density small compared to the kinetic energy density in the flow), it is found that the cocoon formed by lateral expansion of hot, shocked gas from the head of the jet is strongly inhibited. Instead, a magnetically confined “nose cone” of shock processed jet material is formed between the bow shock and Mach disk. In addition, the stability properties of the jet beam itself are strongly altered by the presence of a magnetic field. MHD studies of the propagation of *overdense*, non-radiative jets into a uniform ambient medium which contains a helical magnetic field everywhere have been reported by Todo et al. (1992). They describe results for a number of field strengths and approximate the effects of radiative cooling with an equation of state with $\gamma = 1.2$. The formation of a nose cone, as well as suppression of the cocoon, is evident for strong fields. In subsequent three-dimensional simulations (Todo et al. 1993), it was found that a magnetic field strength of $70\mu\text{G}$ was sufficient to produce nonaxisymmetric kink instabilities in the jet beam which the authors suggest may be relevant to bends observed in the jets from some protostellar systems. This field strength is approaching the value inferred by Morse et al. (1993).

More recently, several authors have reported results from MHD studies of dense jets in which optically thin radiative cooling is directly coupled to the dynamics. Frank et al. (1998, hereafter FRJN-C) report axisymmetric studies which confirm the formation of nose cones, and (for the particular form of the initial field distribution adopted in the jet) the presence of pinch modes driven by magnetic tension. Cerqueira et al. (1997, hereafter CGH; see also de Gouveia Dal Pino & Cerqueira 1996) have used an SPH code which

has been extended with an algorithm designed to represent magnetic forces to study the propagation of dense, cooling jets in three-dimensions. They find that the fragmentation of the dense shell formed by cooling at the head of the jet is strongly affected by magnetic forces, and they use these results to conclude that the clumpy structure observed in jets provides evidence that near the head of the jet the field must be primarily axial rather than helical. In their latest simulations (Cerqueira & de Gouveia Dal Pino 1999, hereafter CG), these authors also report evidence for both modes of the MHD Kelvin-Helmholtz (KH) and a current-driven pinch instability in models of protostellar jets. Finally, Frank et al. (1999a; see also Lery & Frank 1999) have studied the propagation of MHD jets launched by Keplerian accretion disks using analytic models for magneto-centrifugal outflows to describe the jet structure at the nozzle. A variety of complex behavior is seen in this case, some of which results from MHD effects and some which results from the non-uniform radial structure of the jet beam.

Given the apparent sensitivity of jet dynamics to the assumed initial orientation and strength of the magnetic field within the jet beam suggested by published numerical results, it is clearly useful to survey different initial field profiles. In this paper, we present the results from a large number of two-dimensional, axisymmetric MHD simulations of dense, cooling jets. To emphasize the effects produced solely by the magnetic field, we study jets with a uniform (“top-hat”) radial profile propagating into an initially uniform ambient medium. Since the theory of the production of such jets suggests a primarily toroidal field within the outflow far from the source, we focus on toroidal fields with different strengths and radial profiles. In most of our models, the ambient medium into which the jet propagates is unmagnetized, although in some cases we add a poloidal field which threads both the jet and ambient gas initially. Given the importance of nonaxisymmetric instabilities to the dynamics of magnetized jets (Todo et al. 1993), fully three-dimensional MHD simulations of cooling jets are important (CGH; CG), however in order to cover parameter space efficiently we confine the models described in this study to axisymmetry. Moreover, for the highly supermagnetosonic jets studied here, non-axisymmetric modes of, e.g., the K-H instability grow slowly and will not affect the jet in regions close to the nozzle. Of course, precession of the jet beam, a clumpy ambient medium, or a much lower magnetosonic Mach number could introduce three-dimensional effects much earlier. Our results extend previous studies in that we evolve the jet for much longer (using a grid roughly three times larger than used by FRJN-C or CG), and we focus our attention on strongly magnetized jet beams propagating into an unmagnetized ambient medium. Where there is overlap, we compare and contrast our results to previous studies throughout this paper.

The paper is organized as follows. We describe our numerical techniques in §2. As an aid to the interpretation of our results, we review the relevant stability properties of MHD jets in §3. Our results for steady are presented in §4, and for pulsed jets in §5. In §6 we summarize and conclude.

2. Method

2.1. MHD Algorithms

The dynamical evolution of a non-relativistic magnetized jet is given by solutions to the equations of MHD:

$$\frac{D\rho}{Dt} + \rho\nabla \cdot \mathbf{v} = 0, \quad (1)$$

$$\rho \frac{D\mathbf{v}}{Dt} = -\nabla p + (\nabla \times \mathbf{B} \times \mathbf{B})/4\pi \quad (2)$$

$$\rho \frac{D}{Dt} \frac{e}{\rho} = -p\nabla \cdot \mathbf{v} - \Lambda + H, \quad (3)$$

$$\frac{\partial \mathbf{B}}{\partial t} = \nabla \times (\mathbf{v} \times \mathbf{B}). \quad (4)$$

In these equations, $D/Dt = \partial/\partial t + \mathbf{v} \cdot \nabla$ is the convective derivative, Λ and H represent cooling and heating terms, respectively, and the other symbols have their usual meanings. We assume an ideal gas law for the equation of state; that is, $p = (\gamma - 1)e$, where $\gamma = 5/3$, and e is the internal energy density. We adopt the assumptions of ideal MHD in writing equations (1) – (4), in particular we assume the magnetic field is perfectly coupled to the fluid. While temperatures in the jet beam and in the strong shocks at the head of the jet are probably high enough (and therefore the gas is ionized enough) to keep the field well coupled on sub-parsec scales (Frank et al 1999b), it is possible that in slower shocks near the wings of the outflow, non-ideal MHD effects may become important, especially in dense ambient gas. However, the study of non-ideal MHD effects (for example, the structure of “C-type” shocks, Draine & McKee 1993) in the outflow is beyond the scope of this paper.

The second and third terms on the right-hand-side of equation (3) represent energy loss via optically thin cooling and heating respectively. An accurate representation of these terms is one of the most important, and yet challenging, aspects of dynamical studies of cooling jets. Previous work has shown significant differences in the evolution of cooling jets using coronal versus non-equilibrium cooling rates (Stone & Norman 1993). Recently, Raga et al. (1997) have developed an accurate and efficient formulation to approximate non-equilibrium cooling rates in interstellar gas. However, given that the focus of this paper is the effect of magnetic fields on the propagation of cooling jets, we have chosen to adopt only a simple formulation for the optically thin cooling rate: the coronal cooling curve for interstellar gas calculated by Dalgarno & McCray (1972). We allow gas to cool to a temperature of 100 K, below this we set the cooling rate to zero.

We use the ZEUS code (Stone & Norman 1992a; 1992b) to solve the MHD equations in cylindrical coordinates assuming axisymmetry. The stiff cooling and heating terms are differenced implicitly, resulting in a nonlinear equation at every grid point which is solved using a Newton-Raphson iteration scheme. This step is operator split from the rest of the MHD equations. No other additions or modifications to the ZEUS algorithm were required.

2.2. Initial and Boundary Conditions

The axisymmetric simulations are performed on a grid of size $0 \leq r \leq 20R_j$ in the transverse direction, and $0 \leq z \leq 100R_j$ in the axial direction, where R_j is the initial

jet radius. Except where indicated we use 400 uniform zones in the transverse direction and 2000 uniform zones in the axial direction, so that 20 zones span the initial jet radius. Reflecting boundary conditions are used along the inner r boundary, while outflow boundary conditions are used along the outer r , outer z , and inner z boundary for $r > R_j$. For $r \leq R_j$ along the inner z boundary, inflow boundary conditions are used with the variables held fixed at the values appropriate to the initial equilibrium structure of the jet.

Initially the jet is assumed to be perfectly collimated. Motivated by observations of various protostellar jets (e.g., Ray 1996), we adopt the following values as characteristic of observed systems: an initial jet radius $R_j = 2.5 \times 10^{15}$ cm, a uniform density $n_j = 1000 \text{ cm}^{-3}$, and a uniform jet velocity $v_j = 332 \text{ km s}^{-1}$. The gas pressure at the surface of the jet is taken to be $p_0 = 1.38 \times 10^{-10} \text{ dyne cm}^{-2}$, corresponding to a temperature of $T_j = 10^3 \text{ K}$ and sound speed $a_j = 5.25 \text{ km s}^{-1}$. As described below, in order to ensure magnetostatic equilibrium in the radial direction, in some simulations we adopt a radially varying pressure profile. The ambient medium is stationary, with uniform density $n_a = 100 \text{ cm}^{-3}$ (so that the jet is overdense, i.e. $\eta \equiv n_j/n_a = 10$), and temperature $T_a = 50 \text{ K}$. The sound speed in the ambient gas is $a_a = 1.17 \text{ km s}^{-1}$. Note that with these choices, the jet is overpressured with respect to the ambient medium, i.e., $p_a \equiv p_0/\alpha$ and $\alpha = 200$. Several purely adiabatic simulations were performed for comparison with the cooling models, in this case we have taken $p_a = p_0$, $T_a = 10,000 \text{ K}$ and $a_a = 16.6 \text{ km s}^{-1}$, and the jet is initially in pressure equilibrium with the ambient medium. Physically our radiatively cooling models represent a dense jet beam surrounded by a hotter cocoon embedded in a cold ISM. The kinetic model of a dense jet embedded in a less dense cocoon which is in turn ensheathed by a dense and cold molecular gas is consistent with detailed observation of a number of protostellar jet systems including HH111 (Nagar et al. 1997).

Since the strength and orientation of the magnetic field in protostellar jets is not determined observationally, there is considerable freedom in specifying the initial field configuration. We choose to focus on primarily toroidal fields in this paper (although we do present models which include both toroidal and axial fields) as theoretical models of magnetically driven outflows predict the field should become primarily toroidal asymptotically. In the absence of a definitive theory for the radial profile of the magnetic field, we assume the toroidal magnetic field is zero on the jet axis, achieves a maximum at some radial position in the jet interior r_m , and returns to zero at the outer jet boundary. This implies that all currents which support the field are confined within the jet (although as the simulation progresses magnetic field, and therefore current, is convected into the cocoon). Within the jet, we adopt the simple profile for the toroidal magnetic field

$$B_\phi(r) = \begin{cases} B_{\phi,m} \frac{r}{r_m} & 0 \leq r \leq r_m \\ B_{\phi,m} \frac{R_j - r}{R_j - r_m} & r_m \leq r \leq R_j \\ 0 & R_j < r \end{cases} \quad (5)$$

This profile is identical to that used by Lind et al. (1989) and by FRJN-C when $0 \leq r \leq r_m$ and when $r > R_j$ but differs for $r_m \leq r \leq R_j$ where they used a force-free $B_\phi(r) = B_{\phi,m}(r_m/r)$ (which requires a large return current located at the jet surface). CG have studied both longitudinal and helical fields of the form used by Todo et al. (1992) throughout the computational domain. Our toroidal magnetic field corresponds to a uniform current density inside radius r_m , and a distributed return current in the outer portion of the

jet. In adiabatic and cooling jet simulations designed to be compared directly, the toroidal magnetic field reaches a maximum value at $r_m/R_j = 0.9$ with $\beta_1 \equiv \beta_m = 8\pi p_0/B_{\phi,m}^2 = 1$ ($B_{\phi,m} = 58.8 \mu G$) and with $\beta_{1/4} \equiv \beta_m = 0.25$ ($B_{\phi,m} = 117.6 \mu G$). To illustrate the toroidal magnetic field profile adopted here, we plot equation (5) for $\beta_m = 1$ and $r_m = 0.9$ in Figure 1.

The equation of hydromagnetic equilibrium

$$\frac{d}{dr} \left(p_j(r) + \frac{B_z^2(r)}{8\pi} + \frac{B_\phi^2(r)}{8\pi} \right) = -\frac{B_\phi^2(r)}{4\pi r}, \quad (6)$$

has been used to establish a suitable radial gas pressure profile in the jet

$$p_j(r) = \begin{cases} \left\{ 2[1 - (r/r_m)^2] \frac{B_{\phi,m}^2}{8\pi p_0} + p_m/p_0 \right\} p_0 & 0 \leq r \leq r_m \\ \left\{ 1 - \frac{2}{(1-r_m/R_j)^2} \left[3(1 - r/R_j) - (1 - r^2/R_j^2) + \ln(r/R_j) \right] \frac{B_{\phi,m}^2}{8\pi p_0} \right\} p_0 & r_m \leq r \leq R_j \\ p_0 & r = R_j \end{cases} \quad (7)$$

where $p_m = p_j(r_m)$ and

$$p_j(r_m) = p_0 - \frac{2}{(1 - r_m/R_j)^2} \left[3(1 - r_m/R_j) - (1 - r_m^2/R_j^2) + \ln(r_m/R_j) \right] \frac{B_{\phi,m}^2}{8\pi}. \quad (8)$$

The radial pressure profile which gives a magnetostatic equilibrium is shown in Figure 1 where we plot equation (7) for $\beta_m = 1$ and $r_m = 0.9$. Since the jet density is held constant, T_j has the same functional form as p_j . In some of our simulations with strong toroidal fields, the condition of magnetohydrostatic equilibrium within the jet beam requires negative pressures in the neighborhood of r_m . In these cases we simply fix $p_m = 0$, and scale the pressure profile given by equation (7) by an appropriate amount so that this condition is met. Of course, this means that the jet beam is no longer in strict radial equilibrium.

The profile adopted for the magnetic field is an important difference between this work and previous studies (FRJN-C, CG). To allow us to study the effect of the field geometry, we have also performed a few simulations in which the field contains a uniform axial component as well as the toroidal distribution given above, making the field helical. We will also describe the evolution of force-free fields with $B_\phi \propto 1/r$. We find that the detailed structure of a magnetized radiative jet is sensitive to the precise field geometry, thus uncertainty about this geometry is a serious limitation to modeling observed systems.

To construct models of pulsed jets, we apply a purely sinusoidal perturbation in time so the axial component of the velocity is

$$u_z(x=0) = v_j(1 + A \sin \omega t), \quad (9)$$

where we choose $A = 0.25$, and for all of the simulations $\omega = 25a_0/R_j$ where $a_0 = 16.6 \text{ km s}^{-1}$ is a fiducial reference speed (equivalent to the sound speed at a temperature of 10^4 K).

The important dimensionless parameters which characterize the evolution of the jet are the density ratio η (taken to be 10 for all models presented here), and the internal

magnetosonic Mach number $M_{j,ms} = v_j/a_{ms}$, where $a_{ms} \equiv (a_j^2 + V_A^2)^{1/2}$ and V_A is the Alfvén speed. In simulations without toroidal magnetic field or with force-free toroidal magnetic field the pressure, density, and temperature are uniform across the jet, so that the internal sonic Mach number $M_j = v_j/a_j$ is constant. However, a radially varying magnetic pressure requires a radially varying thermal pressure in order to initialize a jet beam in radial force balance and the sonic and magnetosonic Mach numbers are not constant. In general, we characterize all our models by the magnetosonic Mach number on the jet axis. However, since internal dynamics and timescales involve wave propagation across the jet through a medium of varying magnetosonic speed we also define linear radial averages as, for example,

$$\bar{M}_{j,ms} \equiv \frac{1}{R_j} \int_0^{R_j} M_{j,ms}(r) dr. \quad (10)$$

2.3. Tests of the Method

Tests of the MHD algorithms used here have been reported in a number of papers (Stone & Norman 1992a, 1992b; Stone et al. 1992; Hawley & Stone 1995). We have also confirmed that we are able to reproduce the results of previous MHD studies of jets. In particular, we have performed simulations of adiabatic, underdense, magnetized jets using parameters identical to Clarke, Norman, & Burns (1986); we find excellent agreement between our results with those reported by these authors. In particular, we find production of a nose cone with a similar aspect ratio, strong pinch modes within the jet beam due to lack of initial radial equilibrium, and strong suppression of vortical motion in the cocoon by magnetic stresses.

3. Jet stability

Before describing the results of our simulations, let us review the basic stability properties of supermagnetosonic jets in order to aid interpretation. The presence of toroidal magnetic fields and the poloidal current can give rise to current driven pinch modes in addition to velocity shear driven Kelvin-Helmholtz pinch modes. In the absence of any zero order velocity shear, e.g., well inside the velocity shear surface at the jet boundary, Begelman (1998) has shown that a beam containing a toroidal magnetic field can be unstable to current driven pinch modes when

$$\frac{d \ln B}{d \ln r} > \frac{\Gamma \beta(r) - 2}{\Gamma \beta(r) + 2} \quad (11)$$

where the plasma beta $\beta(r) \equiv 8\pi p(r)/B^2(r)$, and Γ is the adiabatic index. In general, shorter pinch lengths will grow faster. If the beam contains a toroidal magnetic field and a weaker uniform axial magnetic field the condition becomes

$$\frac{d \ln B}{d \ln r} > -1 + \frac{1}{2} \left(kr \frac{B_z}{B_\phi(r)} \right)^2, \quad (12)$$

where k is the wavenumber of the mode; in general, shorter pinch lengths, i.e., larger k , are stabilized.

The velocity driven Kelvin-Helmholtz unstable pinch body modes might appear near resonances which, in the absence of radial variation in parameters in the jet and in the external medium, are given by (e.g., Hardee, Clarke, & Rosen 1997; Hardee & Stone 1997)

$$\omega R_j/a_c \approx (2m + 1/2)\pi/2 \quad (12a)$$

$$\lambda/R_j \approx \frac{2\pi}{\omega R_j/a_c} \frac{M_{j,ms}}{1 + M_{j,ms}/M_c} \quad (12b)$$

where ω , m , and λ are the angular frequency, body mode number $m = 1, 2, 3$, etc., and wavelength, respectively. In the expressions above $M_c \equiv v_j/a_c$ and a_c is the sound speed in the cocoon medium immediately outside the jet and not the sound speed in the undisturbed ambient medium. At these resonances the pinch modes grow with spatial growth rate

$$k_I \approx -(2M_{j,ms}R_j)^{-1} \ln(4\omega R_j/a_c), \quad (13)$$

where k_I is the imaginary part of the wavenumber. The spatial growth length over which a linear perturbation increases in amplitude by a factor e is $\ell = |k_I^{-1}| \approx M_{j,ms}R_j$. On the high Mach number axisymmetric flows that we simulate here these Kelvin-Helmholtz modes grow relatively slowly.

4. Steady Jet Simulations

Simulation parameters for the steady jet models discussed here are listed in Table 1. In what follows, we report times in units of a sound crossing time of the jet beam, $\tau_0 \equiv R_j/a_j \approx 152$ yr where $a_j = 5.25$ km s⁻¹. Magnetosonic crossing times of the jet beam are in the range, $\tau_{ms} \equiv R_j/\bar{a}_{ms} \approx 150 - 58$ yr where \bar{a}_{ms} is the linear average of the magnetosonic speed. A grid crossing time can be defined by $\tau_g \equiv L_{grid}/v_h \approx 314$ yr, where $v_h = \left\{ \eta^{1/2} / [1 + \eta^{1/2}] \right\} v_j \approx 250$ km s⁻¹ is the velocity of advance of the head of a cold (thermal and magnetic pressure much less than the ram pressure) jet. We stop the evolution when the bow shock has reached $\sim 100R_j$. The spatial evolution of the jet's transverse structure is then evaluated at an axial distance of $68.5R_j$ (a location behind the region strongly affected by jet head vortices), and the spatial evolution of the cocoon's structure can be evaluated through comparison of cocoon properties at this distance and near to the inlet.

4.1. Magnetized Adiabatic Jets

In order to understand the dynamics of our magnetized radiative jets, it is necessary to first compute non-radiative jet models with an identical magnetic field profile. We have computed three models: a purely hydrodynamical jet (β_∞^{Ad}), a weak field jet (β_1^{Ad}),

and a strong field jet ($\beta_{1/4}^{Ad}$). Table 1 gives additional parameter values adopted for each simulation. Unlike our radiatively cooling jet models, all three adiabatic models are initially in pressure equilibrium with the ambient medium; i.e. we adopt $T_a = 10^4$ K rather than the $T_a = 50$ K used for the cooling jets. Figure 2 plots the logarithm of the density at the end of each of these three simulations. Figure 3 plots the toroidal magnetic field strength B_ϕ at the same times for the two magnetized jet models. Note only the final $50R_j$ of the computational domain is shown in both figures for clarity.

Comparison of the final structure of each jet shows remarkably little difference between these models. In the purely hydrodynamical jet simulation β_∞^{Ad} the jet remains well collimated within its initial radius inside a low density cocoon of typical density one-half the ambient and one-twentieth the jet density, i.e., $n_c \approx 50 \text{ cm}^{-3}$, and has a typical radius $\approx 10R_j$.

The weak toroidally magnetized jet simulation, β_1^{Ad} , experiences some slight collimation from the toroidal magnetic field so that by an axial distance of $68.5 R_j$, where $r_j \lesssim R_j$, the toroidal field maximum has increased by about 7% as it has moved inwards with the contracted jet. However, unlike the β_∞^{Ad} jet we find three significant pressure pulses with amplitudes up to twice $p_j(r)$ and spacing of about $15R_j$ (with the first pulse at an axial distance of $\approx 30R_j$) in the jet interior when $0.1 < r/r_j < 0.6$. The amplitudes are largest at $r \approx 0.3r_j$. This location is not consistent with pressure perturbations produced by the Kelvin-Helmholtz instability at the jet surface. The confinement of these pressure perturbations to the jet interior is consistent with a current driven instability, moreover this region satisfies the condition for instability (eq. [11]) found by Begelman (1998).

The strong toroidally magnetized jet simulation, $\beta_{1/4}^{Ad}$, cannot be introduced at the inlet with a true equilibrium pressure distribution: this would require a negative minimum jet pressure. As a result the jet spine expands to $r_j \approx 1.5R_j$ at an axial distance of $68.5R_j$ and then recollimates somewhat under the influence of higher external pressure near to the jet head and the stronger toroidal magnetic field. At axial distances between $80 - 95R_j$ there is evidence for pressure pulses associated with pinching in the jet interior at $r < 0.2r_j$. Three main pressure pulses with spacing of $\sim 6R_j$ and substructure at one-third this spacing might be due to current driven instability. Neither of the toroidally magnetized adiabatic jet simulations show evidence for a magnetically confined “nose cone” (Clarke, Norman, & Burns 1986; Lind et al. 1989).

4.2. Magnetized Cooling Jets

Images from three cooling jet simulations, a purely hydrodynamical model (β_∞^{Cl}), a weak field model (β_1^{Cl}), and a strong field model ($\beta_{1/4}^{Cl}$) with magnetic field configuration identical to that used in the three adiabatic jet simulations described in §4.1 are shown in Figure 4. Figure 5 shows the toroidal magnetic field strength B_ϕ at the same times for the two magnetized jet models. Note only the final $50R_j$ of the computational domain is shown in both cases. The purely hydrodynamical jet simulation β_∞^{Cl} is directly comparable to the results presented in Stone & Norman (1993; 1994); the primary difference being the use here of the coronal cooling curve of Dalgarno & McCray (1972), as opposed to the

non-equilibrium cooling rates used previously.

Unlike the adiabatic jets discussed above, the addition of a toroidal magnetic field to radiatively cooling jets leads to noticeable differences relative to the non-magnetized β_∞^{Cl} simulation. For example, in β_1^{Cl} the jet beam has expanded in width, and the cocoon is much more uniform and smaller relative to β_∞^{Cl} . Jet expansion in β_1^{Cl} has resulted in a 50% decrease in the toroidal magnetic field strength in the jet beam. No nose cone is evident in either the β_∞^{Cl} or β_1^{Cl} simulations.

The $\beta_{1/4}^{Cl}$ simulation is strongly influenced by expansion of the jet resulting from the non-equilibrium initial configuration at the inlet. Figure 6 plots radial profiles of the density, axial velocity, temperature, and toroidal magnetic field strength at an axial distance of $68.5 R_j$ from the jet nozzle in all three simulations. From the figure, the structure of the $\beta_{1/4}^{Cl}$ jet can be seen to consist of an expanded spine with $r_j \approx 3.5R_j$ surrounded by a sheath of thickness $\approx 3.5R_j$. The magnetic profile shows an approximate linear increase from the axis to $2R_j$ and plateau to $4R_j$ with $B_\phi \approx 21 \mu G$. At the same time, the jet temperature drops from 2,000 K on axis to a low of ~ 100 K in the outer portion of the jet, and then jumps up to $\sim 2,000$ K in the cocoon.

The stronger magnetic field along with jet expansion have resulted in significant morphological changes in jet and cocoon structure beyond an axial distance of about $70 R_j$ in $\beta_{1/4}^{Cl}$. At this distance the jet velocity suddenly decreases by more than a factor of two at an “upstream shock” and a nose cone of length $\approx 25R_j$ is “pushed” ahead of a “downstream shock”. The nose cone drives a more conventional jet terminal and bow shock. The temporal evolution leading to this structure is shown in Figure 7, which plots the logarithm of the density at 5 times during the simulation, $(0.4, 0.8, 1.2, 1.6, 1.8) \times \tau_0 \approx (61, 122, 182, 243, 274)$ yr. Initially the jet remains well collimated. Strong cooling at the head of the jet results in most of the shocked ambient and jet gas collecting in a dense shell ahead of the Mach disk. Once the jet has propagated about $20R_j$, it begins to expand due to lack of magnetohydrostatic balance. Consequently, the head of the jet grows laterally, and becomes filamentary. Most of the shock processed gas is confined to a loosely defined “nose cone” ahead of the Mach disk. Detailed structure at the head of the jet is shown further in Figure 8, which plots the logarithm of the temperature, the divergence of the velocity (an indicator of shocks), and velocity vectors at the end of the simulation. Comparison of the temperature and velocity divergence plots clearly shows that the highest temperatures are located in filaments immediately behind strong shocks in the flow, such as the Mach disk and outer bow shock. Very little non-axial motion is observed in the velocity vectors.

4.3. Cooling Jets with Different Magnetic Field Profiles

Three additional magnetic field profiles have been studied for steady radiatively cooling jets. One simulation, β_{ff}^{Cl} , has a toroidal force-free field in the jet with $B_\phi \propto 1/r$. In this simulation the maximum field strength $B_{\phi,m} = 236.3 \mu G$ ($\beta_m = 0.062$) at $r_m/R_j = 0.05$ (the innermost computational zone) and the magnetic field is set to zero at the jet surface. Within the force-free jet, temperature and thermal pressure are constant. In a second

simulation, β_{Rm}^{Cl} , the magnetic and pressure profiles given by equations (5) and (7) are used with $\beta_m = 0.25$ ($B_{\phi,m} = 117.7 \mu G$) at $r_m/R_j = 0.2$. Unlike the $\beta_{1/4}^{Cl}$ simulation, in this simulation a true equilibrium pressure profile can be achieved and outside the toroidal field maximum the field configuration is not too different from the force free simulation β_{ff}^{Cl} . Finally, a third simulation, $\beta_{\phi z}^{Cl}$, includes an axial magnetic field along with a toroidal magnetic field. In this simulation a constant axial magnetic field in the jet and in the ambient medium of strength $B_z = 58.8 \mu G$ ($\beta_z = 1$) has been added to a toroidal magnetic field profile given by equation (5) with, $r_m/R_j = 0.8$ and $\beta_m = 0.25$ ($B_{\phi,m} = 117.7 \mu G$). In this simulation, the pressure profile in the jet is similar to that in the $\beta_{1/4}^{Cl}$ simulation and is not in equilibrium. Figure 9 plots the logarithm of the density at the final time for each of these simulations (along with the $\beta_{1/4}^{Cl}$ simulation shown in Figures 7 & 8), and Figure 10 plots the corresponding toroidal magnetic field strength. Radial profiles of a variety of quantities in the jet beam for each simulation at an axial distance of $68.5 R_j$ are given in Figure 6.

In β_{ff}^{Cl} the jet cools radiatively and the axial velocity remains constant out to $\sim 90 R_j$ where the velocity abruptly drops by about 20% at a terminal “upstream” shock. A modest nose cone of material about $9 R_j$ in length precedes a “downstream” shock and drives a terminal and bow shock. The jet expands as the initial jet pressure is above the radiatively cooled cocoon pressure at the inlet. The radial structure (Figure 6) is similar in dimension to that found in the β_{∞}^{Cl} and β_1^{Cl} simulations, although the cocoon size is slightly less than in the β_1^{Cl} simulation.

The β_{Rm}^{Cl} simulation serves as an intermediate case between the force-free β_{ff}^{Cl} simulation and the non force-free $\beta_{1/4}^{Cl}$ simulation, and can also be compared to the β_1^{Cl} simulation. Inside the jet when $r > 0.2r_j$ the magnetic field profile is very similar to the force-free case. At the inlet the jet is overpressured relative to the radiatively cooled cocoon but jet expansion does not begin until an axial distance of about $40 R_j$. Interior to this distance nine well defined pressure oscillations with a spacing of $\sim 3.3 R_j$ are observed at jet radii $r < 0.15r_j$, and probably are the result of a current driven pinch mode. Pressure fluctuations attributable to this pinch mode are on the order of $\pm 2\% - 3\%$ and these fluctuations disappear as the jet begins to expand. At an axial distance of $68.5 R_j$ (Figure 6) the jet spine and sheath are reduced in size by about 25% relative to the force-free configuration. The jet is in approximate pressure balance with the cocoon at this point. We note that the jet spine contains a relatively high pressure and temperature central region confined by the magnetic field. The cocoon is also reduced in size by about 25% relative to the force-free configuration. A modest nose cone about $10 R_j$ long leads the jet in this case after a velocity drop of 15% in an “upstream” shock.

Finally in the $\beta_{\phi z}^{Cl}$ simulation we consider the effect of adding an axial magnetic field to the toroidal magnetic field configuration used in $\beta_{1/4}^{Cl}$. The axial field imposed over the entire computational grid has served to ameliorate the large jet expansion observed in $\beta_{1/4}^{Cl}$ and at an axial distance of $68.5 R_j$ (see Figure 6) the jet spine $r_j \approx 3R_j$ and sheath of thickness $\approx R_j$ together equal the jet spine width in $\beta_{1/4}^{Cl}$. This width is similar to that seen for the β_{ff}^{Cl} jet and in this simulation the jet is at lower pressure than the hotter cocoon. Toroidal magnetic field resides within the jet spine and sheath, while the axial magnetic

field has been reduced within the jet by jet expansion but increased by compression in the outer part of the cocoon. This additional magnetic field and accompanying high sheath and higher cocoon density has helped to confine the jet. The presence of axial magnetic field has almost but not quite eliminated the extensive nose cone observed in the $\beta_{1/4}^{Cl}$ simulation.

5. Pulsed Jets

Some of the most prominent structural features in highly collimated jets associated with protostellar objects are the bright emission knots in the flow close to the source (see Reipurth 1997 for a recent review of the observations). It has been suggested that symmetric pinch modes of the Kelvin-Helmholtz (K-H) instability might give rise to such knots (Bührke, Mundt, & Ray 1988), which has motivated detailed hydrodynamical modeling of the nonlinear evolution of symmetric K-H modes in cooling jets (Massaglia et al. 1992; Bodo et al. 1994; Rossi et al. 1997; Downes & Ray 1998). However the large proper motion observed in some cases (Eislöffel & Mundt 1994), and direct kinematic evidence provided by spectroscopic observations (Reipurth 1997) have shown that some knots are associated with velocity variability in the outflow. Thus, while the nonlinear stage of *nonaxisymmetric* modes of the K-H instability might still prove relevant to understanding the helical structures or wiggles observed in some protostellar jets (Hardee & Stone 1997; Stone, Xu, & Hardee 1997), most of the internal knot structure in the jets is probably produced by flow variability in the jet beam.

The hydrodynamics of velocity-variable, or pulsed, jets has been widely studied in the literature (see Raga 1993 for a review). In an important early contribution, Raga & Kofman (1992) demonstrated that a sinusoidal velocity variation at the jet inlet steepens into a sawtooth pattern downstream. One-dimensional (Hartigan & Raymond 1993), followed by multidimensional hydrodynamical simulations (Stone & Norman 1993; de Gouveia Dal Pino & Benz 1994; Biro & Raga 1994; Biro 1996; Suttner et al. 1997) have shown that the velocity discontinuities in the sawtooth pattern consist of a shock pair: an upstream shock decelerating high velocity gas as it collides with the pulse, and a downstream shock sweeping up low velocity material ahead of the pulse. These shock pairs move apart at a constant rate causing the pulse width to grow linearly in time up to some asymptotic value. In the absence of magnetic fields this evolution can be understood by a simple analytic model (Falle & Raga 1993). Recently, there has been considerable effort in understanding how such “internal working surfaces” (Raga et al. 1990) affect the dynamics and observed properties of jets. In this section, we present the results of an investigation of the magnetohydrodynamics (MHD) of radiatively cooling pulsed jets.

Parameters for the simulations discussed below are listed in Table 2. Because shock compression on the downstream and upstream sides of pulses generated by velocity fluctuation is a function of jet radius, we include in Table 2 area weighted averages as, for example,

$$\langle M_{j,ms} \rangle \equiv \frac{2}{R_j^2} \int_0^{R_j} M_{j,ms}(r) r dr . \quad (13)$$

5.1. Variation in Magnetic Field Strength

We have computed a purely hydrodynamic model with $\beta_\phi = \infty$, hereafter denoted as β_∞^P , to serve as a benchmark. Two simulations were performed using a toroidal magnetic field profile in the jet beam given by equation 5 in Paper II, with $r_m = 0.9R_j$. The first model has a peak field strength of $B_{\phi,m} = 58.8\mu G$ corresponding to an equipartition field, i.e. $\beta_{\phi,m} \equiv 8\pi p_0/B_{\phi,m}^2 = 1$, hereafter denoted as β_1^P . The second model has a peak field strength $B_{\phi,m} = 117.6\mu G$ corresponding to a strong field where $\beta_{\phi,m} = 0.25$, hereafter denoted as $\beta_{1/4}^P$. These profiles are identical to those adopted in the steady jet simulations β_∞^{Cl} , β_1^{Cl} , and $\beta_{1/4}^{Cl}$.

In Figure 11 we show images of the logarithm of the density at the final time in the three simulations. The β_∞^P model is directly comparable to previous results of hydrodynamical simulations, e.g., Stone & Norman (1993). Despite the use of a different numerical method (a PPM algorithm was used in this earlier work, instead of the ZEUS code used here) and lower numerical resolution, there is excellent agreement in the overall structure of the jet. The steepening of the sinusoidal pulses into thin, dense sheets by $z \approx 10R_j$ is evident. Thereafter, the pulses are bounded by two shocks. Significant mass flux into the cocoon from the high pressure shocked gas within the pulse is evident as smooth flows. Each pulse is seen to drive a shock into the cocoon, so that the cocoon is much broader than steady jet models using the same parameters. The structure at the head of the jet is complex as pulses begin to merge with one another, and interact with the ambient medium. Note that the pulse width increases linearly with distance from the nozzle. For the purely hydrodynamic jet, the rate of increase in size is set by the balance between radial mass loss into the cocoon from the pulse “surface” and the mass flux into the pulse through isothermal shocks (Falle & Raga 1993).

As the magnetic field strength is increased (models β_1^P and $\beta_{1/4}^P$ shown in the lower two panels of Figure 11), the gross properties of the pulsed jet remain the same. Two features of the pulses are clearly modified by the magnetic field. Firstly, the postshock density within the pulses on the axis increases with the field strength. Secondly, the rate of increase in the pulse width increases with increasing magnetic field strength. While the presence of hoop stresses associated with the toroidal field clearly influences the amount of material ejected from the pulses into the cocoon, the maximum radial distance that material is ejected into the cocoon does not decrease with field strength. In all three simulations, the wings generated by the pulses extend to a radial distance of $\sim 5R_j$. Figure 12 plots the logarithm of the toroidal magnetic field strength in β_1^P and $\beta_{1/4}^P$. The field acts as a tracer of jet material since the ambient gas is unmagnetized. Compression of the magnetic field by the internal shocks associated with the pulses, and ejection of material and the magnetic field into the cocoon is evident. Note this ejection occurs over a larger area in $\beta_{1/4}^P$ as might be expected given the larger pulse width.

In order to illustrate the variation of properties of the pulses with magnetic field strength, we plot in Figure 13 the density, pressure, axial velocity, and toroidal magnetic field strength along an axial slice through the center of all three jets at time $t = 1.2\tau_0$ – note that this time is not the same as that used in Figures 11 and 12. Only a limited segment of the axial domain between $20R_j$ and $45R_j$ is shown for clarity. The plot shows three pulses developing within this region, one centered near $23R_j$, the next at $31R_j$, and the last at $38R_j$. In both cases the magnetic field strength declines outwards from the

origin over the region shown in Figure 13 by a factor 2 – 3. Several trends are clearly evident in the plot. Note the increase in width of the pulses with axial distance. The strongly magnetized model shows the widest pulses. Interestingly, the gas pressure is nearly identical within all three jets. The axial density is much higher in the strongly magnetized pulsed jet, increasing from 5 times (in the first pulse) to 20 times (in the last pulse) larger than the hydrodynamic pulsed jet. The axial velocity shows the classic sawtooth pattern expected for a sinusoidally pulsed jet (Raga & Kofman 1992), modified by the shock pair which appears at each step (e.g., Stone & Norman 1993). The toroidal field strength follows the density profile closely as would be expected in ideal MHD when the magnetic field is parallel to the shock interface.

In all three jets, the pulse width increases linearly with axial distance. At $z \sim 50R_j$, the pulse widths are about $4R_j$, $5R_j$, and $7R_j$ in β_∞^P , β_1^P , and $\beta_{1/4}^P$, respectively. To zeroth order the linear growth rate in the pulse width scales with $1/\langle M_{j,ms} \rangle$ rather than the sound speed (Falle & Raga 1993) (see Table 2). In β_1^P and β_∞^P the pulses remain separated along the entire length of the jet, so that the upstream and downstream shock pair is evident nearly to the jet head. On the other hand, the spreading of the pulse width is so large in the $\beta_{1/4}^P$ model that the pulses merge before reaching the head of the jet, leading to the disappearance of the upstream shock – leaving only a sequence of downstream shocks – at $z > 60R_j$.

The observed differences in pulse density, radial density profile and pulse width are the result of hoop stresses which confine some of the shocked jet material within the pulses to near the axis, and the result of the lack of radial pressure equilibrium in the material after it passes through the upstream and downstream shocks into the pulse. Recall that the unshocked material in β_1^P is in radial pressure equilibrium. In an isothermal shock the toroidal magnetic pressure increases $\propto \rho^2$ whereas thermal pressure increases $\propto \rho$. Thus, in general, the toroidal plasma β behind the shocks should decrease relative to the toroidal plasma β in the unshocked jet material by up to $\propto \rho^{-1}$. Of course, the toroidal plasma β in the unshocked and shocked pulse material is a function of radius and the relative importance of thermal versus magnetic pressure is further modified by material and magnetic ejection from the pulse. However, in $\beta_{1/4}^P$ the area weighted plasma β in a typical pulse is $\langle \beta_\phi \rangle \lesssim 2$ (compared to $\langle \beta_\phi \rangle \sim 8$ in the unshocked jet material), and in this case magnetic pressure can play a significant role in supporting the pulses against ram pressure.

Considerable toroidal field accumulates at the head of the jet into a nose-cone-like structure; this is most evident in the very strong field case. For our parameters typical magnetic field strengths in the pulses at $z > 20R_j$ are about $50\mu\text{G}$ and $75\mu\text{G}$ in β_1^P and $\beta_{1/4}^P$, respectively, and the field strength declines as the distance from the inlet increases. Between the pulses the magnetic field strength is reduced from these values by over a factor of 10. Near the head of the jet in the complex interactions between shocked jet material ejected from the pulses and shocked ambient gas, field strengths are as high as $190\mu\text{G}$ in β_1^P , and $570\mu\text{G}$ in $\beta_{1/4}^P$.

5.2. Radial Variation in Magnetic Field and Pulse Structure

We have studied the effect of varying the geometry of the magnetic field in the jet beam using three different simulations. The first, β_1^P , is the model discussed above in which $B_{\phi,m} = 58.8\mu G$ at $r = 0.9R_j$. The second, β_{Rm}^P , is another equipartition toroidal magnetic field model but with $B_{\phi,m} = 58.8\mu G$ at $r = 0.2R_j$. The third, $\beta_{\phi z}^P$, is a model with $B_{\phi,m} = 58.8\mu G$ at $r = 0.8R_j$, and which contains a uniform axial field of $B_z = 58.8\mu G$, with $\beta_z \equiv 8\pi p_0/B_z^2 = 1$ added throughout the computational domain. In all three of these simulations, the jet beam is initially in exact radial equilibrium.

Images of the logarithm of the density at the final time in each of these simulations are shown in Figure 14. A comparison between β_1^P and β_{Rm}^P shows that when the magnetic field is peaked close to the axis, the pulses widen non-uniformly, growing in width more rapidly near the axis of the jet than at the surface. The size and shape of the wings of the pulses is similar in both models. A strong axial magnetic field (model $\beta_{\phi z}^P$) helps to confine material in the pulses and reduces the amount of material ejected to the cocoon.

Images of the logarithm of the toroidal magnetic field strength in β_1^P , β_{Rm}^P , and $\beta_{\phi z}^P$ are shown in Figure 15. In β_1^P , considerable toroidal magnetic field has been injected into the cocoon. Since the field tracks jet material, this indicates a large amount of shocked jet gas is ejected from the pulses. On the other hand, in β_{Rm}^P the strongest toroidal field is found close to the axis, and there is much less magnetic field in the cocoon, indicating reduced ejection of shocked jet material from the pulses. In $\beta_{\phi z}^P$ the toroidal magnetic field is more confined towards the axis indicating that considerably less material is ejected from the pulses into the cocoon, and the cocoon is smaller in this simulation than in the other two simulations.

In Figure 16 we plot various quantities as a function of radius for pulses at an axial distance $z/R_j = 48, 53, 51, 47.5$ and 51 at the final time in simulations β_∞^P , β_1^P , $\beta_{1/4}^P$, β_{Rm}^P and $\beta_{\phi z}^P$, respectively. These locations are the centers of last pulse which is non-interacting with its neighbors at the final time in each simulation. Note that $\beta_{1/4}^P$ and β_{Rm}^P result in similar axially peaked density pulse profiles (although the axial density in $\beta_{1/4}^P$ is four times that in β_{Rm}^P). Other magnetic field configurations are less axially peaked but are still very different from the “top hat” profile of the hydrodynamical simulations (solid line in each panel). In all cases the magnetized pulses are significantly colder on the axis, typically by more than a factor of 2, than the hydrodynamic pulse. The hydrodynamic pulse has a “top hat” temperature profile with $T_{pulse} \approx 1,300$ K. Expansion velocities evaluated at $r = 0.8R_j$ lie within $\pm 15\%$ of a_j ($a_j = a_0/3.16$) and are relatively independent of magnetic field strength or configuration. Thus, we might expect an equilibrium pulse width (mass into the pulse through upstream and downstream shocks balanced by transverse mass ejection) to scale approximately proportional to the density at the $r = 0.8R_j$ surface, i.e., with the mass ejection rate per unit surface area evaluated at $r = 0.8R_j$.

At least approximately we would expect the pulse expansion rate and ultimate width in β_1^P and $\beta_{\phi z}^P$ to be comparable but twice that (and in $\beta_{1/4}^P$ and β_{Rm}^P comparable but about four times that) observed in the hydrodynamic case. Our simulations do in fact show an increase in the rate at which pulses widen consistent with this analysis, although the rate of this increase is not as fast as this simple argument would predict.

From Figure 16, the maximum radial ejection velocity from the pulses occurs at a radial distance much larger than the pulse surface at $r = 0.8R_j$. It is affected by the magnetic field configuration and strength, with the highest velocities observed for the strongest toroidal magnetic field case, $\beta_{1/4}^P$, and lowest velocities observed when an axial magnetic field is present, $\beta_{\phi z}^P$. Changes to the unshocked toroidal plasma β in the pulses is also dependent on the magnetic field configuration and strength, and the radial variation in β_ϕ shown in Figure 16 is much different from that at the inlet (see Table 2). If we characterize the effects of the magnetic field by the area weighted toroidal plasma β then we find that $\langle\beta_\phi\rangle_{pulse} \approx \langle\beta_\phi\rangle_{jet}$ in cases β_1^P and $\beta_{\phi z}^P$, whereas $\langle\beta_\phi\rangle_{pulse} \ll \langle\beta_\phi\rangle_{jet}$ in cases $\beta_{1/4}^P$ and β_{Rm}^P . Note that this properly groups the magnetic simulations with their observed spreading rates. However, only in case $\beta_{1/4}^P$ where $\langle\beta_\phi\rangle_{pulse} \sim 1.5$ can there be significant magnetic pressure effects. We conclude that the differences in pulse width spreading rate are the result of the radial density profile in the pulse induced by radial pressure equilibrium with B_ϕ , and clearly the density profile is significantly modified even when the area weighted toroidal plasma β is much greater than one.

6. Summary

6.1. Steady Jets

Although inclusion of a weak magnetic field (weak in the sense that the flow is highly supermagnetosonic) has little effect on the propagation of adiabatic, overdense jets (e.g. Figures 2 and 3), such fields have strong effects on cooling, overdense jets (e.g. Figures 4, 5, 9 and 10). The difference is caused by the much larger compression of jet and ambient gas that occurs in cooling shocks. This compression amplifies the magnetic field until in some cases the magnetic pressure is comparable to the gas pressure in shocked gas, a situation which never occurs in the adiabatic jet simulations.

Our simulations reveal at least three effects of the magnetic field on steady, cooling jets. Firstly, the field affects the structure and fragmentation of dense sheets of cooled gas (e.g. Figures 4 and 9). This is in part because magnetic pressure can support cooling gas against compression, and so limit the density and width of cooling shells. Alternatively, magnetic stresses can inhibit the radial flow of gas away from the axis, leading to higher densities in some cases. Both of these effects are evident in comparison of models β_∞^{Cl} , β_1^{Cl} , and $\beta_{1/4}^{Cl}$ (Figure 4). The structure of the magnetic field is important to its overall effect, for example, helical magnetic fields appears to produce smoother fluctuations in the cocoon than purely toroidal fields of the same strength (see Figure 9). Much of this may be attributed to the difference the field has on the radial structure of the jet, either through expansion or compression of the jet beam by pressure and hoop stresses. Jets which undergo radial expansion have a much larger cross section near their tip, and drive larger, more fragmented shells into the ambient gas. Jets which are confined or compressed by the magnetic field tend to have narrower and smoother cocoons.

Secondly, the presence of a magnetic field can, in some cases, result in the production of a dense, plug of shocked jet material ahead of the Mach disk (a “nose cone”). The formation

of nose cones has been noted previously in simulations of magnetized extragalactic jets (Clarke et al. 1986). However, we find the formation of nose cones in cooling jets is sensitive to the geometry of the field: only purely toroidal fields which peak near the surface of the jet form nose cones, simply because this configuration maximizes the hoop stresses which confine the nose cone. Moreover, nose cones are likely to be unstable in 3D which will limit their relevance to real protostellar jets.

Finally, the presence of magnetic fields affects the stability of the jet beam. We do not observe any evidence for the MHD K-H instability in our simulations, nor do we expect to given that the linear growth rates for such modes are small for the supermagnetosonic jets studied here. Interestingly, we observe axial pressure fluctuations in a few simulations where the jet beam is unstable to current driven pinch modes (Begelman 1998). However, our simulations reveal such modes saturate at low amplitude in the nonlinear regime, so that it is unlikely they will have much relevance to the internal knots observed in most protostellar jets.

6.2. Pulsed Jets

Our simulations reveal that weak magnetic fields have a number of effects on time-variable (pulsed) cooling jets. Such pulsing results in the formation of dense knots of shocked jet material in the jet beam. The inclusion of a toroidal magnetic field affects the rate at which such knots grow by inhibiting the radial flow of material out of the knots and into the cocoon. This results in much higher densities in the pulses as the field strength is increased (Figure 13). The *increase* of the density in the cooling gas in the shocked pulses as the magnetic field strength is increased contradicts the expectations of simple planar shock theory: this result emphasizes the importance of multidimensional effects in MHD flows.

A second effect of a non-uniform magnetic field is the introduction of radial structure into the density and pressure of the pulses, even if the jet is uniform at the nozzle. Jets with strong toroidal fields have radial density profiles in the pulses which are strongly peaked toward the axis. This profile is introduced by radial variations in the magnetic pressure and hoop stresses in the shocked pulses, which confines material near the axis. It is unlikely that real protostellar jets have a uniform (“top-hat”) profile: it has been shown that the structure of the cocoon can be affected by the profile of the density and velocity in the jet beam through hydrodynamical simulations (Suttner et al 1997). Our results reinforce the importance of understanding the radial profile of the outflow to interpret the structures observed.

Finally, even though toroidal fields affect the internal radial structure of the pulses, we do not observe much effect on the structure of the cocoon due to the magnetic field. Radial profiles of various quantities in the pulses (Figure 16) show that the *maximum* axial velocity of material ejected from the pulses into the cocoon is relatively insensitive to the field strength. Thus, the size of the cocoon is not significantly decreased in the magnetized jets. The radial ejection velocity is small (a few times the sound speed in the unperturbed jet beam), and it would require a delicate force balance to completely eliminate radial outflow.

7. Conclusions

We have studied the propagation of both steady and time-variable (“pulsed”) protostellar jets using numerical MHD simulations. Although we focus our attention on models in which the jet beam contains a purely toroidal magnetic field peaked near its surface, we have also studied the effect of varying both the strength and geometry of the field on the dynamics.

We find that even a weak magnetic field ($B \leq 60\mu\text{G}$) in the jet beam can lead to important effects on the structure and dynamics of steady jets (FRJN-C; CGH; CG). In particular, such fields can alter the density structure and fragmentation of dense shells formed in cooling jets. However, the details of the effects depend sensitively on the geometry of the field. For example, while magnetic pressure can limit compression in such shells, resulting in *lower* densities and less fragmented shells, radial hoop stresses associated with purely toroidal fields can confine shocked gas towards the axis, resulting in *higher* densities there. In some cases, hoop stresses lead to the formation of nose cones ahead of the Mach disk. We see no evidence for significant structure induced by the Kelvin-Helmholtz instability (such modes were seen for the parameters and field geometry adopted by CG). We do see evidence for current driven pinch modes but the induced pressure pulses in the jet interior do not appear strong enough to explain the emission knots that are observed in protostellar jets (see also CG). Thus, models invoking jet velocity fluctuation appear to remain the most viable explanation for the knots observed in protostellar outflows. We do not see any evidence for disruption of the jet by pinch modes.

In the case of pulsed cooling jets, we find the primary effect of a toroidal magnetic field is to confine shocked jet material to the axis, preventing it from being ejected into the cocoon, and leading to higher postshock densities in the pulses in comparison to purely hydrodynamic models. This result is in contrast to the expectation of planar radiative shock models, in which the addition of a magnetic field leads to *lower* postshock densities. Our results indicate it is important to account for multidimensional effects in the study of magnetized cooling jets. Toroidal confinement also leads to radial variation of quantities in the pulses, even if the density and velocity initially are constant with radius. The radial variation of, e.g. the density, in the pulses is large enough (a factor of 80 in a strongly magnetized jet) that it will likely affect the computation of the resulting emission properties.

While there are many uncertainties in the magnetic field strength and topology implied by the observations, our present results make it clear that MHD models of protostellar jets need to be seriously investigated. This is particularly true since we find that average values of the magnetic field which correspond to a plasma β much larger than one (and which therefore one would infer to be too weak to be important) can still make a significant difference in the dynamics and physical conditions associated with the jet, and therefore its emission properties as well. It is thus important to understand the asymptotic structure of the field produced by the mechanism which drives the outflow.

We thank E. de Gouveia Dal Pino for comments on an earlier version of the manuscript, and an anonymous referee for suggested improvements. JS acknowledges support from the DOE through grant DFG0398DP00215. PH acknowledges support from the National Science Foundation through grant AST-9318397 and AST-9802955 to the University of Alabama.

REFERENCES

- Begelman, M.C. 1998, ApJ, 493, 291
- Biro, S. 1996, MNRAS, 278, 990
- Biro, S., & Raga, A. 1994, ApJ, 434, 221
- Bodo, G., Massaglia, S., Ferrari, A., & Trussoni, E., 1994, A&A, 283, 655
- Bürke, T., Mundt, R., & Ray, T.P. 1988, A&A, 200, 99
- Cabrit, S., Raga, A.C., & Gueth, F., 1997, in IAU Symp. 182, Herbig-Haro Flows and the Birth of Low Mass Stars, ed. by B. Reipurth & C. Bertout, (Kluwer:Dordrecht), p. 163
- Cerqueira, A.H., de Gouveia Dal Pino, E.M., & Herant, M., 1997, ApJ, 489, L185 (CGH)
- Cerqueira, A.H., & de Gouveia Dal Pino, E.M., 1999, ApJ, 510, 828 (CG)
- Clarke, D.A., Norman, M.L., & Burns, J.O., 1986, ApJ, 311, L63
- Clarke, D.A., 1996, in ASP Conf. Ser. 100, Energy Transport in Radio Galaxies and Quasars, ed. by P.E. Hardee, A.H. Bridle, & J.A. Zensus (San Francisco: ASP), 311.
- Dalgarno, A., & McCray, R.A. 1972, ARA&A, 10, 375
- Downes, T.P., & Ray, T.P., A&A, 331, 1130
- Draine, B.T., & McKee, C.F., 1993, ARA&A, 31, 373
- Eislöffel, J., & Mundt, R., 1994, A&A, 284, 530
- Frank, A., Ryu, D., Jones, T.W., Noriega-Crespo, A., 1998, ApJ, 494, L79 (FRJN-C)
- Frank, A., Lery, T., Gardiner, T., Jones, T., & Ryu, D., 1999a, preprint.
- Frank, A., Gardiner, T., Delemarter, G., Lery, T., & Betti, R., 1999b, ApJ524, 947
- de Gouveia Dal Pino, E.M., & Benz, W. 1994, ApJ, 435, 261
- de Gouveia Dal Pino, E.M., & Cerqueira, A.H., 1996, Astron. Lett. Comm., 34, 303
- Falle, S.A.E.G., & Raga, A.C. 1993, MNRAS, 261, 573
- Hardee, P.E., Clarke, D.A., & Rosen, A. 1997, ApJ, 485, 533
- Hardee, P.E., Norman, M.L., Koupelis, T., & Clarke, D.A. 1991, ApJ, 373, 8
- Hardee, P.E., & Stone, J.M., 1997, ApJ, 483, 121
- Hartigan, P., & Raymond, J., 1993, ApJ, 409, 705
- Hawley, J. F. & Stone, J. M. 1995, Comput Phys Comm, 89, 127
- Königl, A., & Pudritz, R., 1999, to appear in *Protostars and Planets IV*, ed. by V. Manning, A. Boss, & S. Russell (U. Arizona Press:Tucson)
- Kössl, D., Müller, E., & Hillebrandt, W., 1990a, A&A, 229, 378
- Kössl, D., Müller, E., & Hillebrandt, W., 1990b, A&A, 229, 401
- Lery, T., & Frank, A., 1999, preprint.
- Lind, K., Payne, D., Meier, D., & Blandford, R.D., 1989, ApJ, 344, 89
- Massaglia, S., Trussoni, E., Bodo, G., Rossi, P., & Ferrari, A., 1992, A&A, 260, 243
- Morse, J.A., Heathcote, S., Cecil, G., Hartigan, P., & Raymond, J.C. 1993, ApJ, 410, 764

- Nagar, N.M., Vogel, S.N., Stone, J.M., & Ostriker, E.C., 1997, ApJ, 482, L195
Ostriker, E.C., 1997, ApJ, 486, 291
Raga A.C., Canto, J., Binette, L., & Calvet, N., 1990, ApJ, 364, 601
Raga, A.C. & Kofman, L. 1992, ApJ, 386, 222
Raga, A.C., 1993, Ap&SS, 208, 163
Raga, A.C., 1995, Rev. Mex. Astr. Astrof. Ser. Conf., 1, 103
Raga, A.C., Mellema, G., & Lundqvist, P., 1997, ApJS, 109, 517
Ray, T.P., 1996, in Proceedings of the NATO ASI on Solar and Astrophysical MHD Flows, ed. K. Tsinganos (Dordrecht: Kluwer), in press
Ray, T.P., Muxlow, T., Axon, D., Brown, A., Corcoran, D., Dyson, J., & Mundt, R., 1997, Nature, 385, 415
Reipurth, B., 1997, in *Herbig-Haro Flows and the Birth of Stars; IAU Symposium No. 182*, ed. by B. Reipurth & C. Bertout, (Kluwer), p. 3.
Rossi, P., Bodo, G., Massaglia, S., & Ferrari, A., 1997, A&A, 321, 672
Shu, F., Najita, H., Shang, Z., & Li, Z.-Y., 1999, to appear in *Protostars and Planets IV*, ed. by V. Manning, A. Boss, & S. Russell (U. Arizona Press:Tucson)
Suttner, G., Smith, M.D., Yorke, H.W., & Zinnecker, H., 1997, A&A, 318, 595
Stone, J. M., & Norman, M. L. 1992a, ApJS, 80, 753
Stone, J. M., & Norman, M. L. 1992b, ApJS, 80, 791
Stone, J.M., Hawley, J.F., Evans, C.E., & Norman, M.L. 1992, ApJ, 385, 415
Stone, J.M., & Norman M.L. 1993, ApJ, 413, 198
Stone, J.M., & Norman M.L. 1994, ApJ, 420, 237
Todo, Y., Uchida, Y., Sato, T., & Rosner, R., 1992, PASJ, 44, 245
Todo, Y., Uchida, Y., Sato, T., & Rosner, R., 1993, ApJ, 403, 164

8. Figure Captions

Fig. 1.— Radial profile of the toroidal magnetic field (solid line) and thermal pressure (dashed line) in the jet beam.

Fig. 2.— Images of the logarithm of the density at the final time in adiabatic overdense jets with no magnetic field $-\beta_\infty^{Ad}$ – (top panel), and weak $-\beta_1^{Ad}$ – (middle panel) or strong $-\beta_{1/4}^{Ad}$ – (bottom panel) toroidal field. A linear color scale between $\log n = 0.97$ and 4.32 is used, where n is the particle number density in cm^{-3} . The maximum density in each case is $\log n = 4.05$, 4.32 and 3.48 , respectively. The initial density of the jet and ambient medium are $\log n_j = 3$ and $\log n_a = 2$. The axes are labelled in units of the initial jet radius; note only the last $50R_j$ of the computation is shown in each case. For typical protostellar jet parameters, $\tau_0 = 152$ yrs and $100R_j = 0.08$ pc.

Fig. 3.— Images of the logarithm of B_ϕ for the magnetized jets shown in Figure 2. A linear color map between $\log(B_\phi/\sqrt{4\pi}) = -2$ and 1.1 is used. The maximum values are $\log(B_\phi/\sqrt{4\pi}) = 0.54$ and 1.1 , respectively.

Fig. 4.— Images of the logarithm of the density at the final time in cooling overdense jets with no magnetic field $-\beta_\infty^{Cl}$ – (top panel), and weak $-\beta_1^{Cl}$ – (middle panel) or strong $-\beta_{1/4}^{Cl}$ – (bottom panel) toroidal field. A linear color scale between $\log n = 0.30$ and 5.6 is used. The maximum density in each case is $\log n = 4.2$, 5.6 and 5.4 , respectively.

Fig. 5.— Images of the logarithm of B_ϕ for the magnetized jets shown in Figure 4. A linear color map between $\log(B_\phi/\sqrt{4\pi}) = -2$ and 1.4 is used. The maximum values are $\log(B_\phi/\sqrt{4\pi}) = 1.16$ and 1.4 , respectively.

Fig. 6.— Radial profiles of density, axial velocity, temperature, and toroidal magnetic field in cooling steady jet simulations at $z \sim 68.5R_j$ from β_∞^{Cl} (solid), β_1^{Cl} (dotted), $\beta_{1/4}^{Cl}$ (long

dash), β_{ff}^{Cl} (dot long dash), β_{Rm}^{Cl} (dot short dash), and $\beta_{\phi z}^{Cl}$ (short dash). The density, axial velocity, and temperature are scaled relative to the ambient density, ρ_a , the fiducial speed, a_0 , and temperature $T_0 = 10,000$ K.

Fig. 7.— Time history of the logarithm of the density during the propagation of an overdense, cooling, strongly magnetized jet. A linear color scale between $\log n = -0.06$ and 5.4 is used.

Fig. 8.— Logarithm of the temperature (top panel), velocity divergence (middle panel), and velocity vectors (bottom panel) near the head of the overdense, cooling, strongly magnetized $\beta_{1/4}^{Cl}$ jet, at time $1.8\tau_0 \approx 274$ yrs. A linear color map is used for the temperature between $\log T = 1.87$ and 5.8. Only negative velocity divergence values are shown, sharp filaments indicate the location of shocks in the flow. The maximum length of velocity vectors is scaled to 350 km s^{-1} .

Fig. 9.— Images of the logarithm of the density at the final time in cooling overdense jets. Top panel: a strong toroidal field – $\beta_{1/4}^{Cl}$ – which peaks at $r = 0.9R_j$. Second panel: a strong toroidal field – β_{Rm}^{Cl} – which peaks at $r = 0.2R_j$. Third panel: a strong toroidal field – $\beta_{\phi z}^{Cl}$ – which peaks at $r = 0.9R_j$ combined with a weak axial field. Bottom panel: a force-free toroidal field – β_{ff}^{Cl} . A linear color scale between $\log n = 0.36$ and 5.4 is used. The maximum density in each case is $\log n = 5.36, 4.93, 4.33$ and 5.36, respectively. From top to bottom the jets are shown at times of $1.8\tau_0, 1.8\tau_0, 1.7\tau_0$, and $1.7\tau_0$ respectively

Fig. 10.— Images of the logarithm of B_ϕ for the magnetized jets shown in Figure 9. A linear color map between $\log(B_\phi/\sqrt{4\pi}) = -2$ and 1.5 is used. The maximum values are $\log(B_\phi/\sqrt{4\pi}) = 1.37, 1.22, 1.22$ and 1.49, respectively.

Fig. 11.— Images of the logarithm of the density at the final time for the pulsed jets: β_∞^P – no magnetic field – (top panel), β_1^P – equipartition toroidal field – (middle panel), and

$\beta_{1/4}^P$ – strong toroidal field – (bottom panel). A linear color scale between $\log n = -1.4$ and 5.3 is used, where n is the number density in cm^{-3} . The maximum density in each case is $\log n = 4.46, 4.65,$ and 5.29 respectively. The initial density of the jet and ambient medium is $\log n_j = 3$ and $\log n_a = 2$ respectively. The axes are labelled in units of the initial jet radius; note the vertical scale is expanded by a factor of two for clarity.

Fig. 12.— Images of the logarithm of B_ϕ for the magnetized pulsed jets β_1^P and $\beta_{1/4}^P$ shown in Figure 11. A linear color map between $\log(B_\phi/\sqrt{4\pi}) = -2$ and 1.3 is used. The maximum values are $\log(B_\phi/\sqrt{4\pi}) = 1.2$ and 1.3 , respectively.

Fig. 13.— Axial profiles along the axis ($r = 0$) of density, pressure, velocity, and magnetic field for pulsed jets β_∞^P (solid line), β_1^P (dotted line) and $\beta_{1/4}^P$ (dashed line) at $t = 1.2\tau_0$. Only the region between $20R_j$ and $45R_j$ from the jet nozzle is shown.

Fig. 14.— Images of the logarithm of the density at the final time for the pulsed jets: $\beta_{1/4}^P$ – strong toroidal field peaked at $r_m = 0.9R_j$ – (top panel), β_{Rm}^P – equipartition toroidal field peaked at $r_m = 0.2R_j$ – (middle panel) and $\beta_{\phi z}^P$ – equipartition toroidal field peaked at $r_m = 0.8R_j$ and a uniform axial field – (bottom panel). A linear color scale between $\log n = -2.1$ and 4.9 is used. The maximum density in each case is $\log n = 4.65, 4.86,$ and 4.35 respectively. Note the vertical scale is expanded by a factor of two for clarity. From top to bottom the jets are shown at times of $1.6, 1.6,$ and $1.7\tau_0$ respectively.

Fig. 15.— Images of the logarithm of B_ϕ for the magnetized pulsed jets $\beta_{1/4}^P, \beta_{Rm}^P,$ and $\beta_{\phi z}^P$ shown in Figure 14. A linear color map between $\log(B_\phi/\sqrt{4\pi}) = -2$ and 1.3 is used. The maximum values are $\log(B_\phi/\sqrt{4\pi}) = 1.2, 1.3,$ and 1.1 , respectively.

Fig. 16.— Radial profiles of density, radial velocity, thermal pressure, and toroidal plasma β in pulses at $z \sim 50R_j$ from β_∞^P (solid line), β_1^P (dotted line), β_{Rm}^P (dashed-dotted line), $\beta_{\phi z}^P$ (short dashed line), and $\beta_{1/4}^P$ (long dashed line). The density, radial velocity, and thermal

pressure are scaled relative to the ambient density, ρ_a , the fiducial speed a_0 , and the inlet thermal pressure at the jet edge, p_0 .

TABLE 1
Simulation Parameters For Steady Jets

Simulation	$M_{j,ms}^{(a)}$	$\bar{M}_{j,ms}^{(b)}$	$M_{a,ms}$	$P_j^{(a)}/P_0$	r_m/R_j	$\beta_{\phi,m}^{(c)}$	$\beta_z^{(c)}$
β_{∞}^{Ad}	63.2	63.2	20	1	—	—	—
β_1^{Ad}	43.9	48.3	20	2	0.9	1	—
$\beta_{1/4}^{Ad}$	22.4	25.5	20	8	0.9	0.25	—
β_{∞}^{Cl}	63.2	63.2	283	1	—	—	—
β_1^{Cl}	43.9	48.3	283	2	0.9	1	—
$\beta_{1/4}^{Cl}$	22.4	25.5	283	8	0.9	0.25	—
β_{ff}^{Cl}	14.1	30.1	283	1	0.05	0.062	—
β_{Rm}^{Cl}	19.2	42.0	283	11	0.2	0.25	—
$\beta_{\phi z}^{Cl (d)}$	20.9	24.5	18.3	8	0.8	0.25	1

^a on jet axis in first computational zone

^b linear average

^c $\beta = 1$ corresponds to $B = 58.8\mu G$

^d 10 zones/ R_j

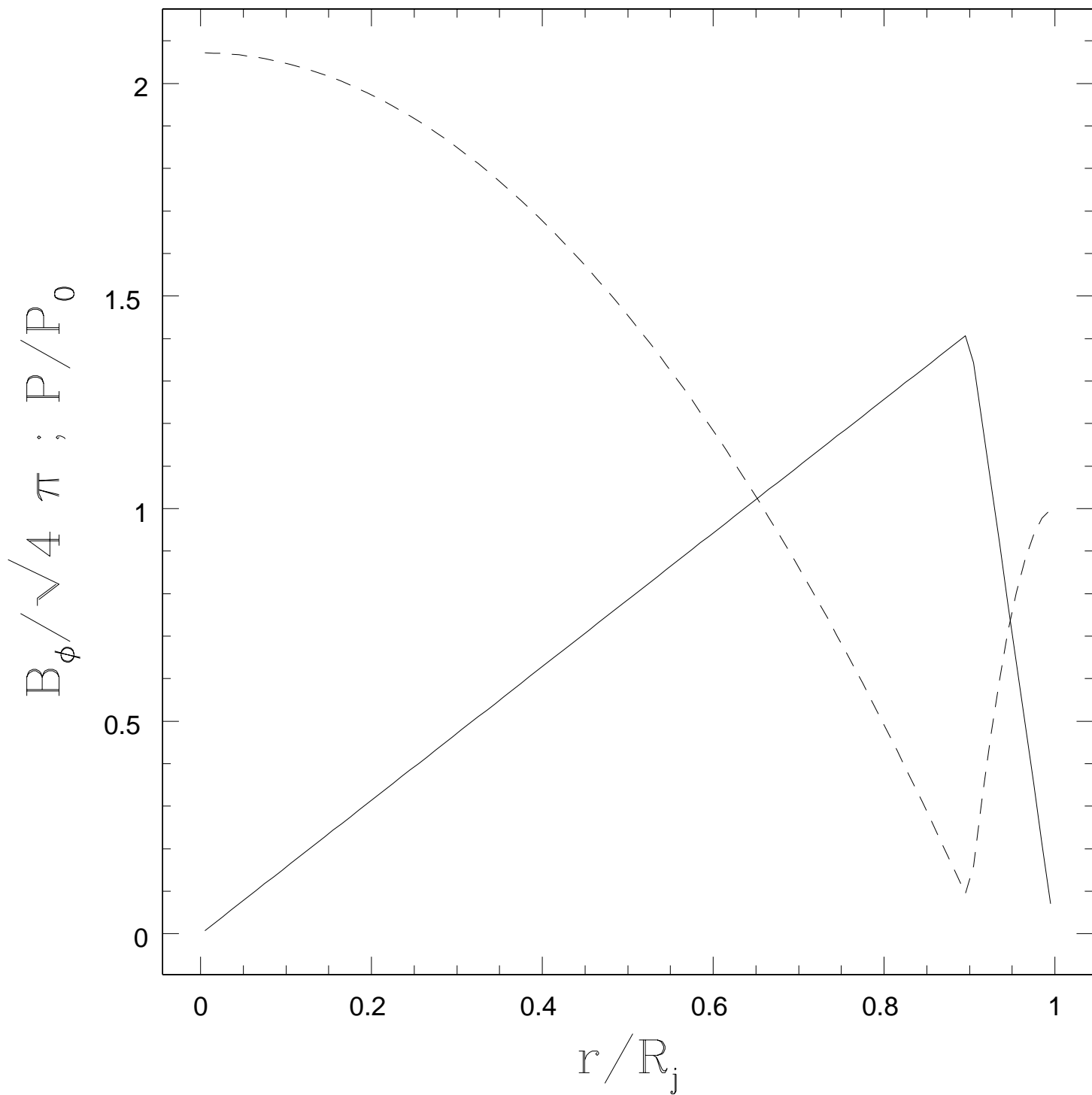
TABLE 2
Simulation Parameters For Pulsed Jets

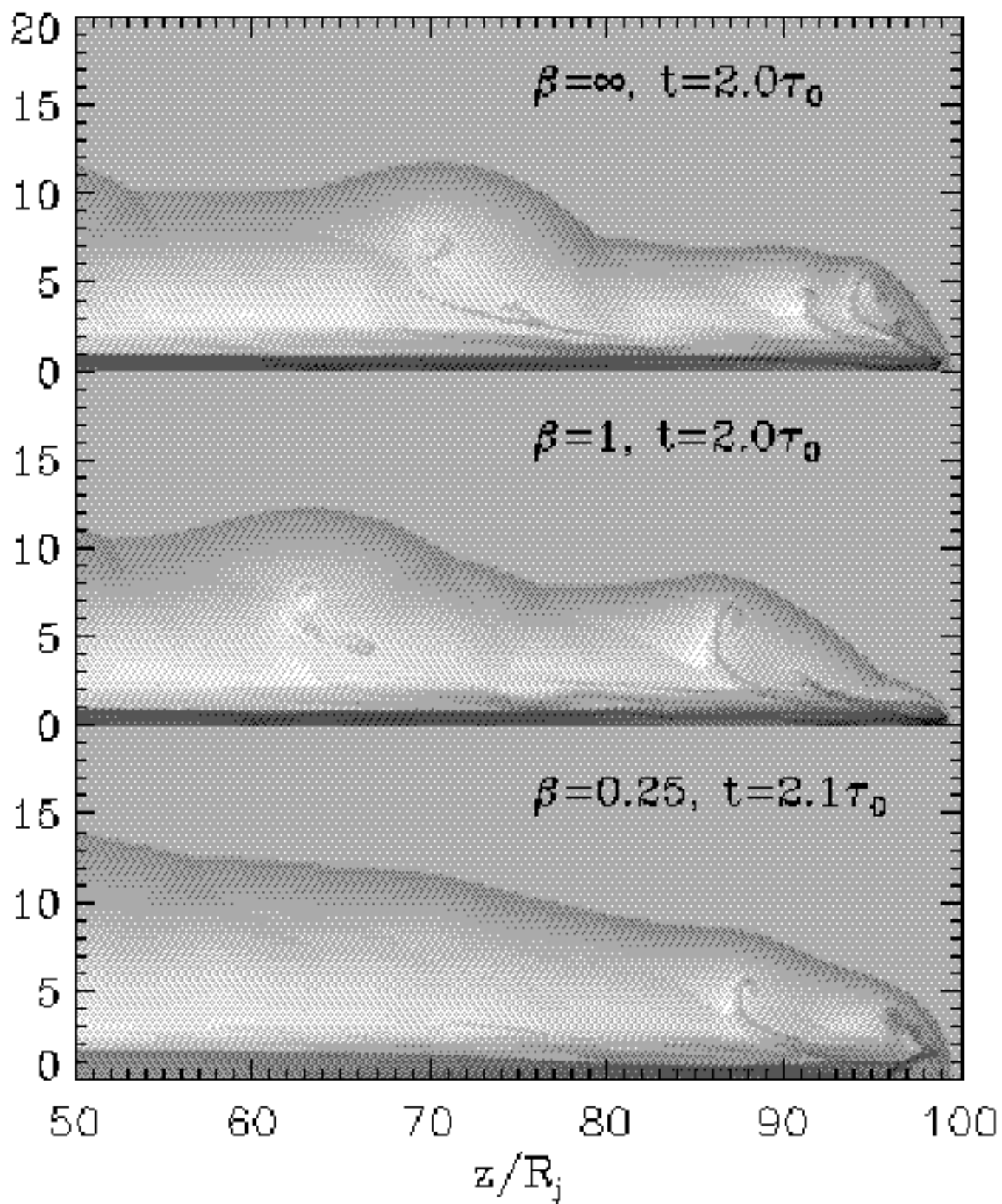
Simulation	$M_{j,ms}^{(a)}$	$\langle M_{j,ms} \rangle^{(b)}$	$\langle M_{j,s} \rangle^{(b)}$	$M_{a,ms}$	$P_j^{(a)}/P_0$	r_m/R_j	$\beta_{\phi,m}^{(c)}$	$\beta_z^{(c)}$	$\langle \beta_\phi \rangle^{(b)}$
β_∞^P	63.2	63.2	63.2	283	1	—	—	—	∞
β_1^P	43.9	50.5	68.9	283	2	0.9	1	—	6.7
$\beta_{1/4}^P$	22.4	27.3	46.4	283	8	0.9	0.25	—	8.2
β_{Rm}^P	33.6	57.2	60.7	283	3.5	0.2	1	—	16.4
$\beta_{\phi z}^P$	34.5	38.3	64.6	18.3	2.2	0.8	1	1	10.2

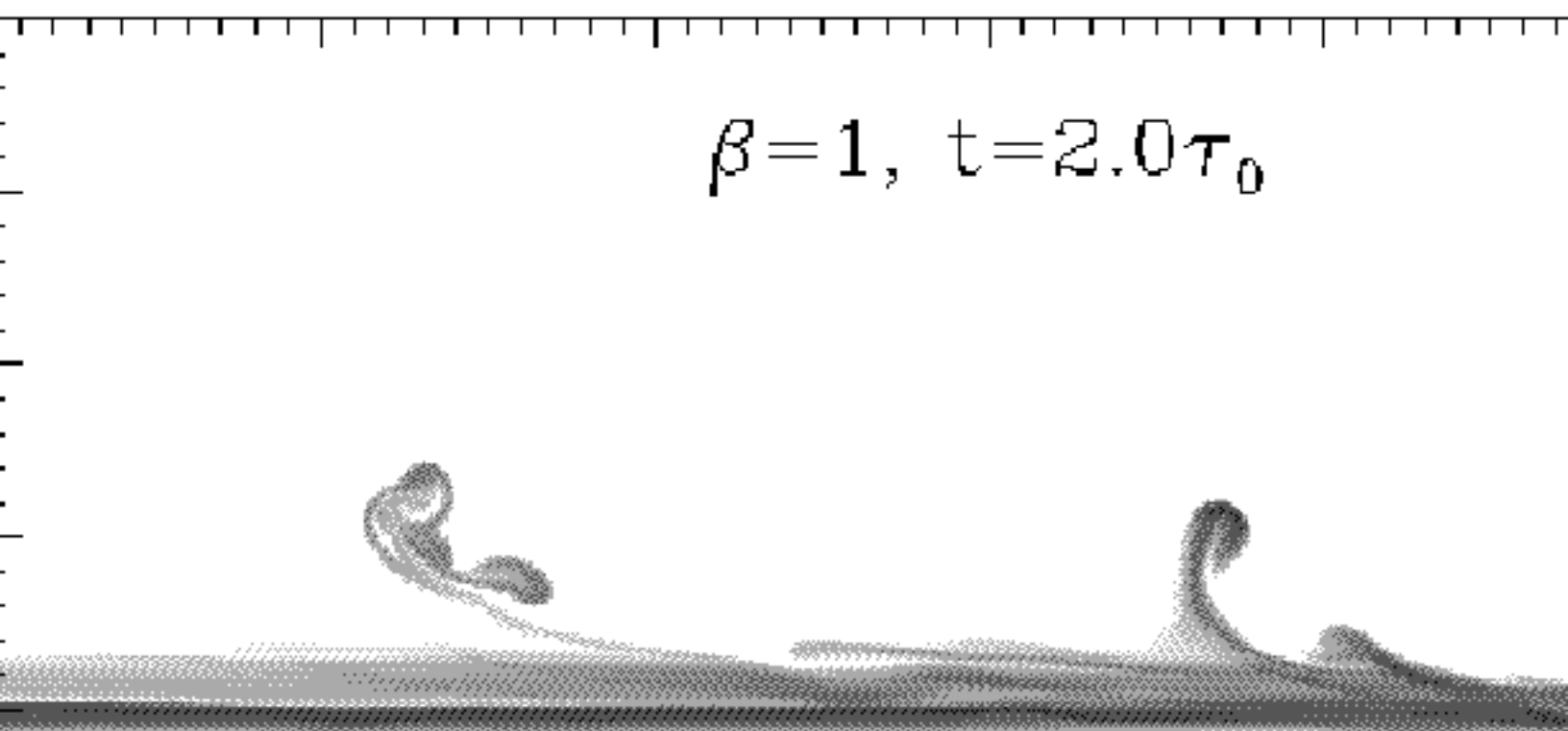
^a on jet axis in first computational zone

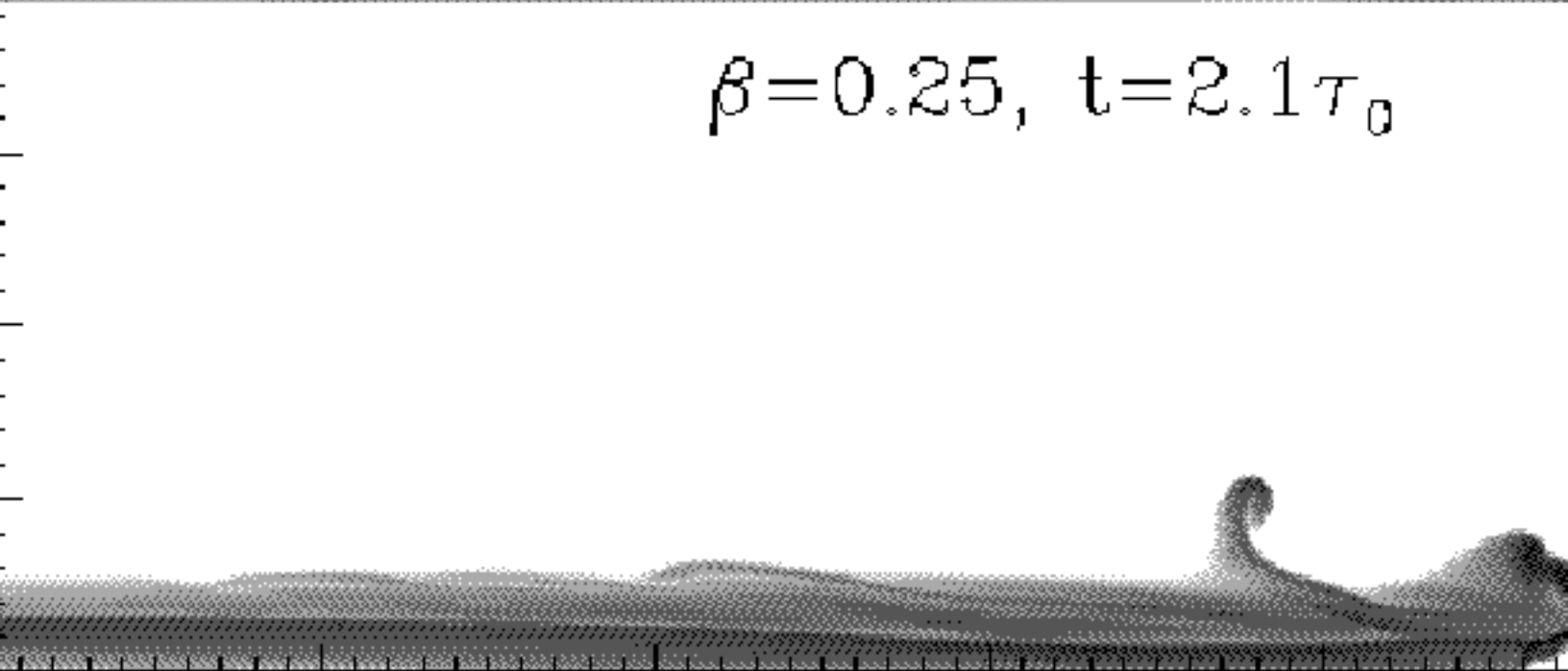
^b area weighted average

^c $\beta = 1$ corresponds to $B = 58.8\mu G$






$$\beta = 1, t = 2.0\tau_0$$


$$\beta = 0.25, t = 2.1\tau_0$$

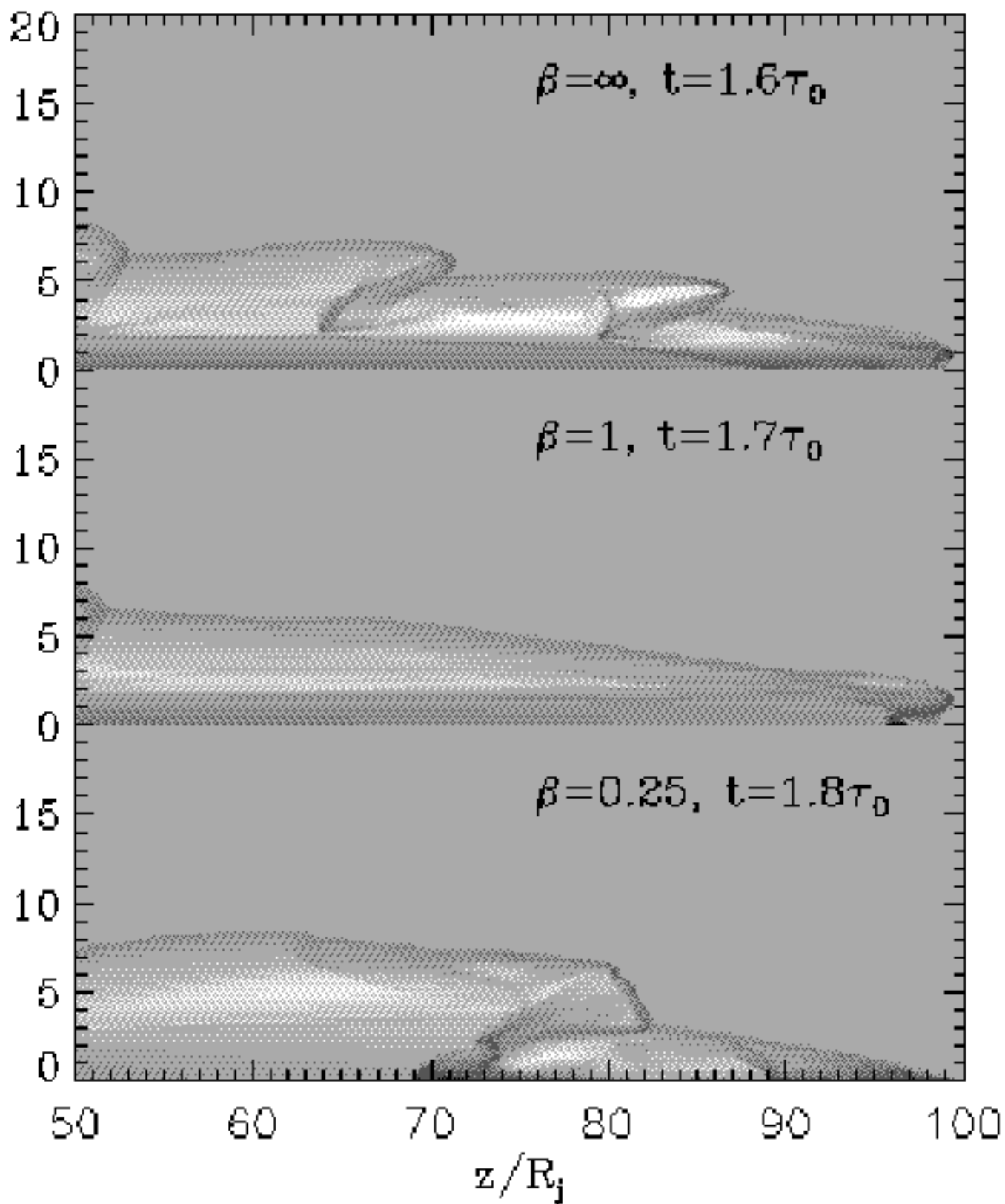
60

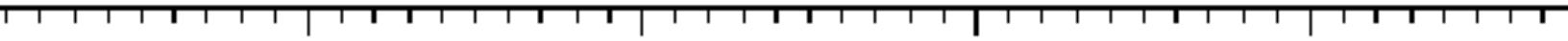
70


80

90

 z/R_j




$$\beta = 1, t = 1.7\tau_0$$


$$\beta = 0.25, t = 1.8\tau_0$$

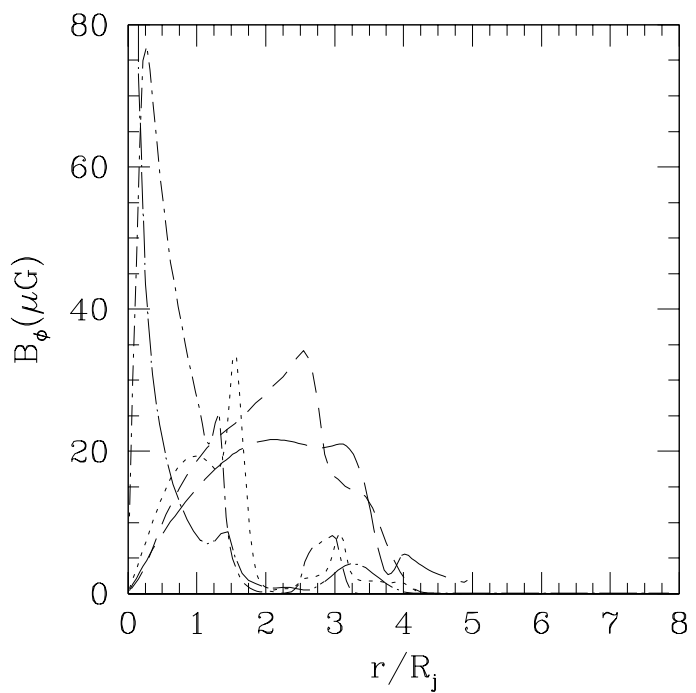
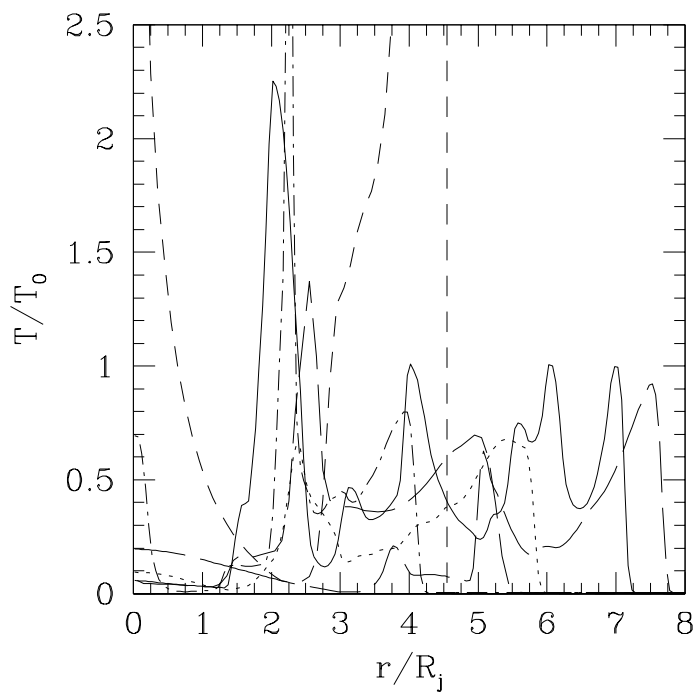
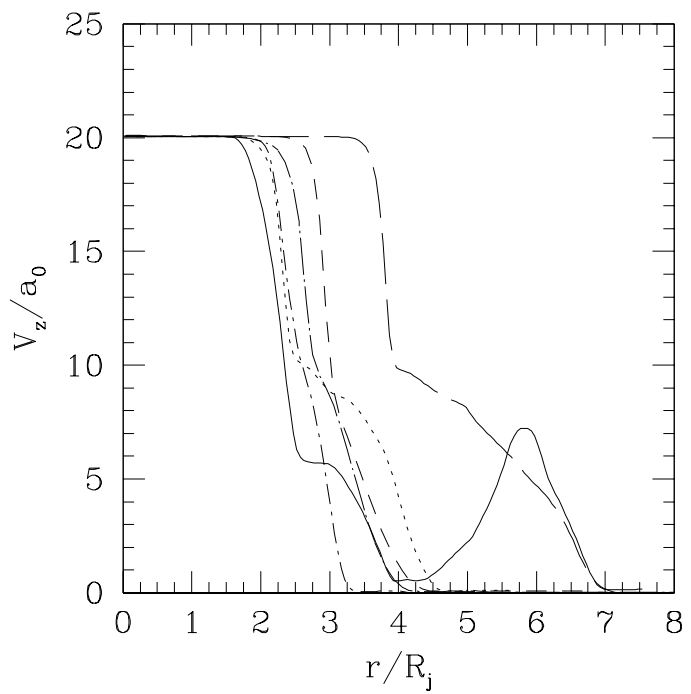
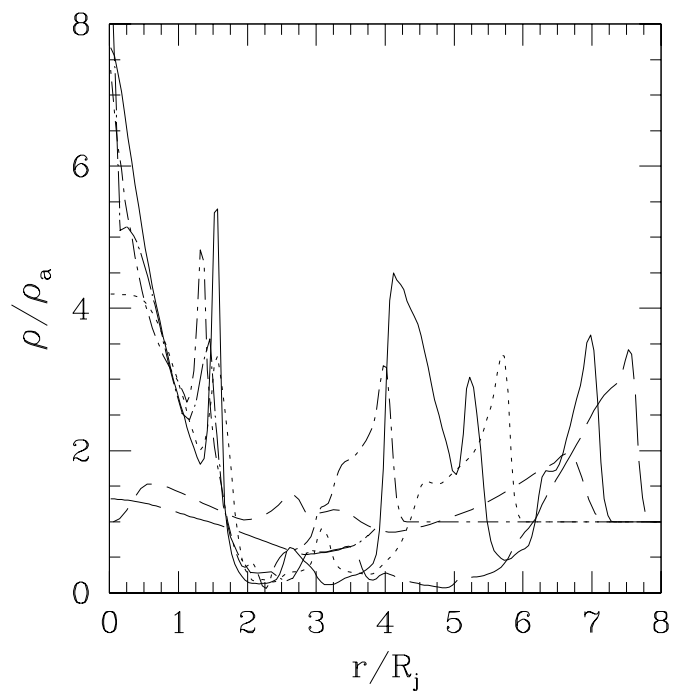
60

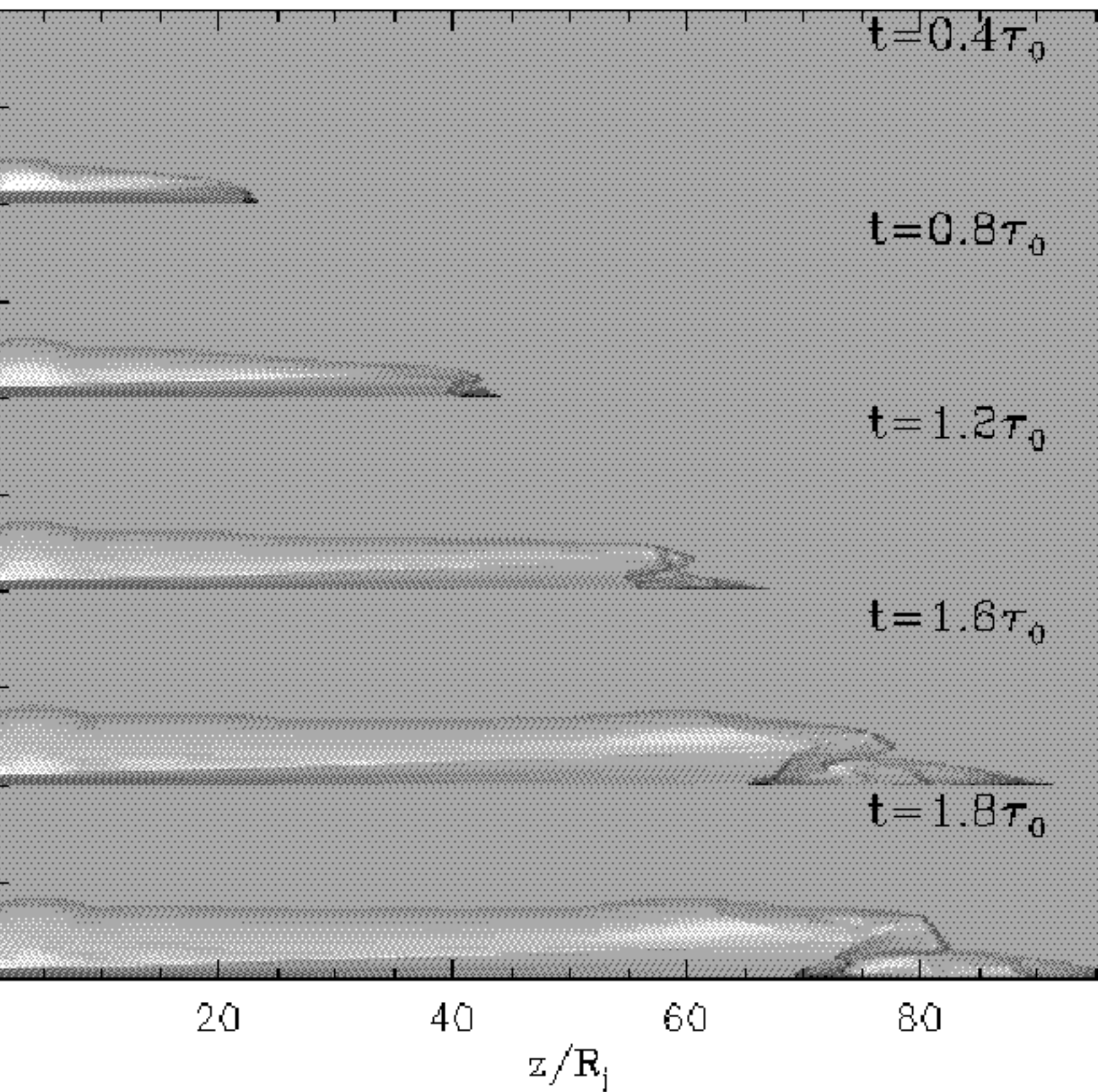
70

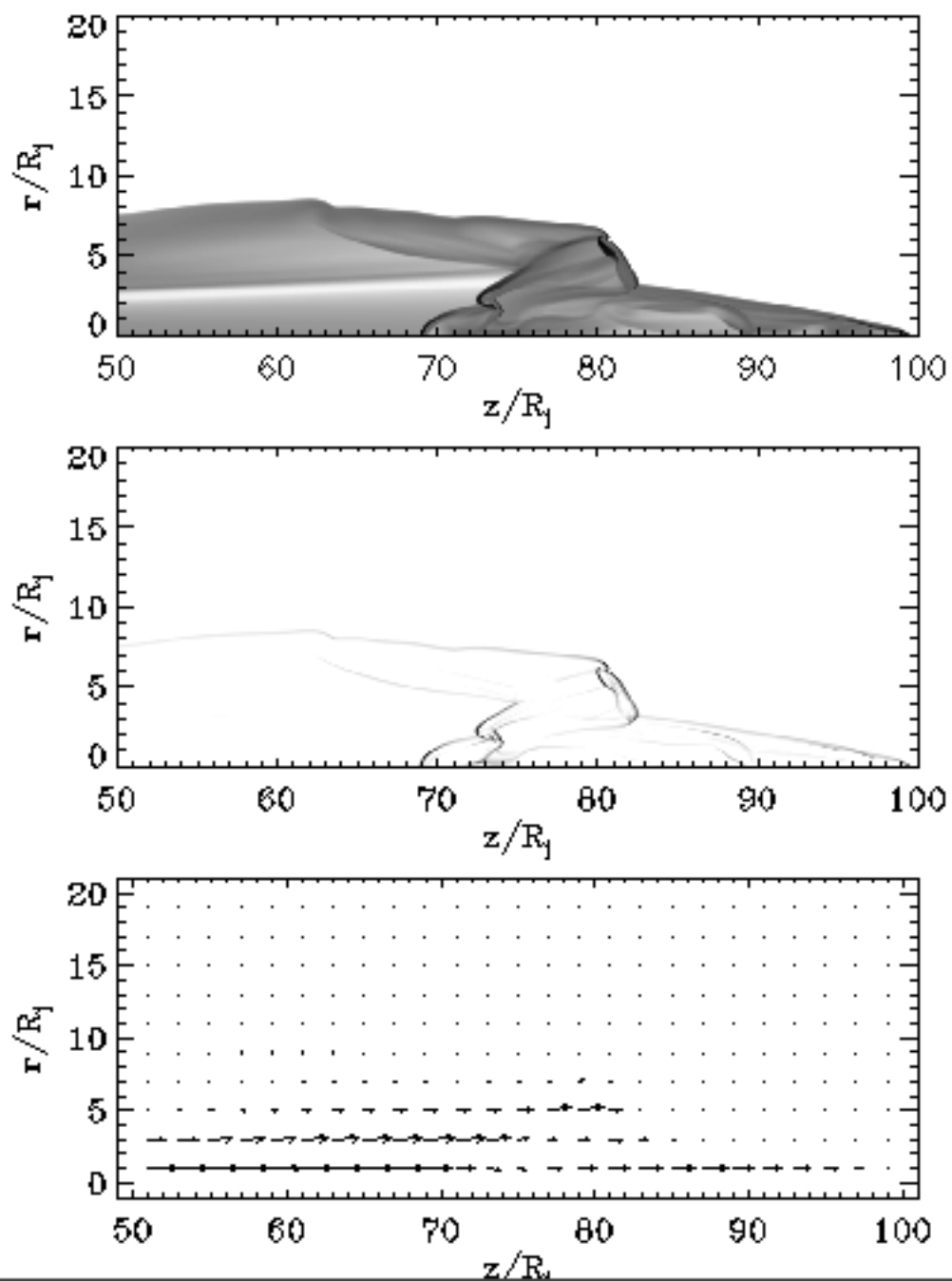
80

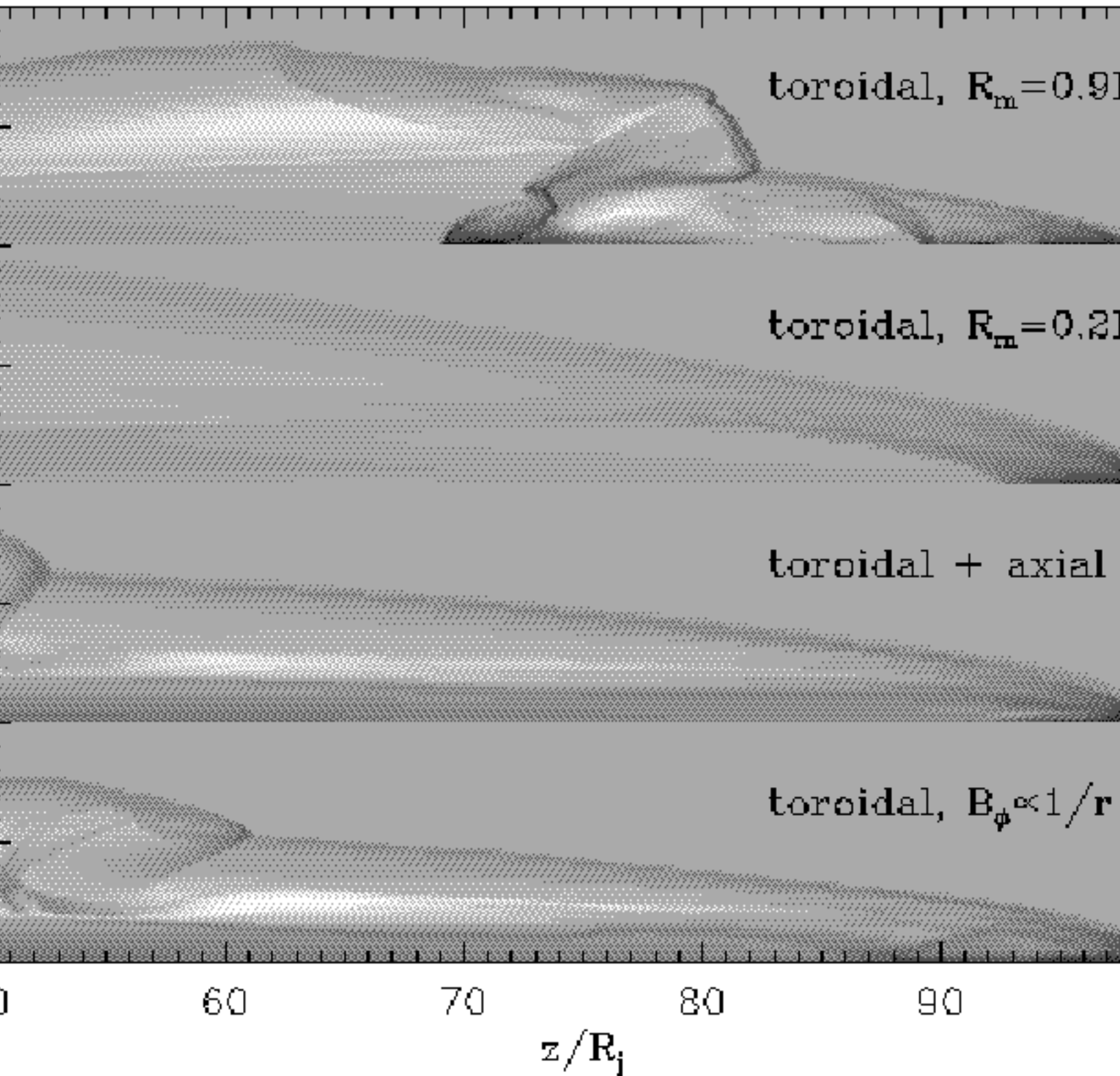
90

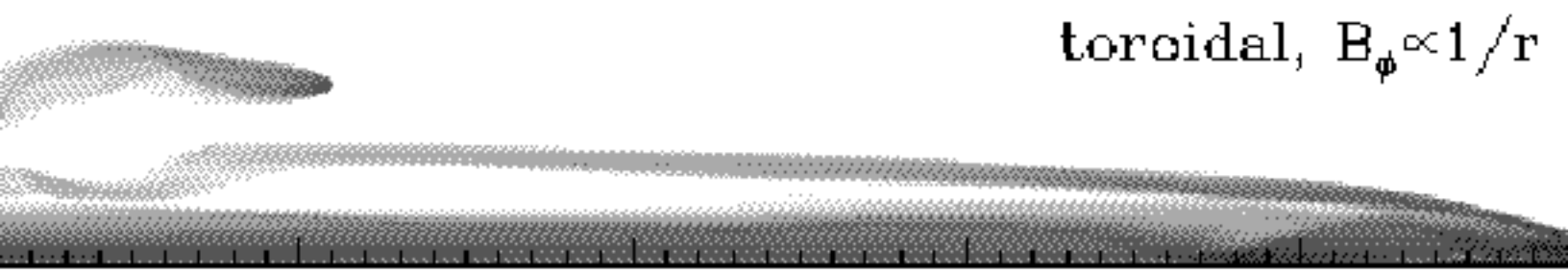
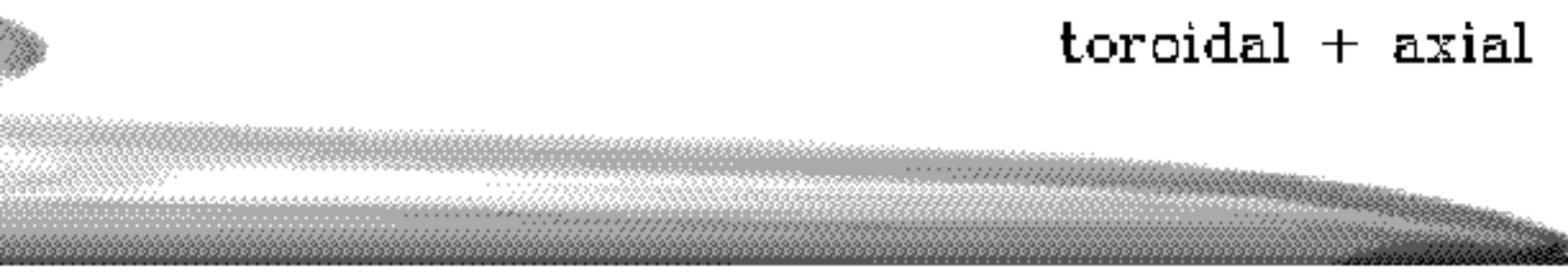
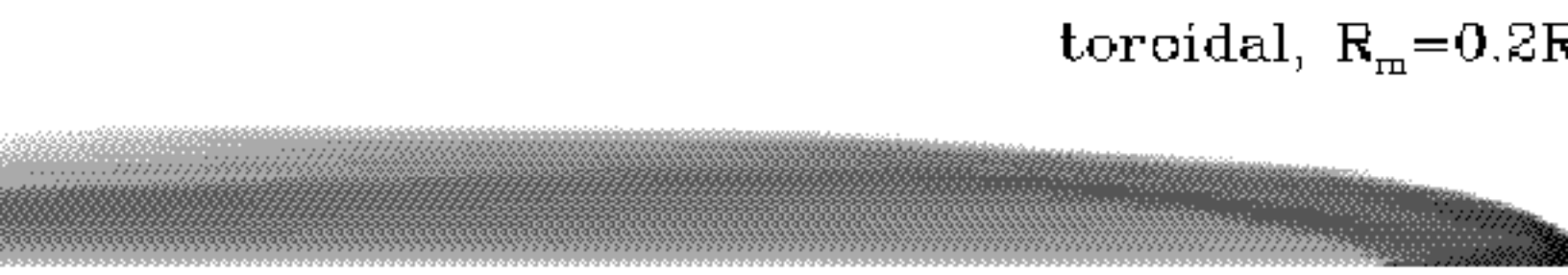
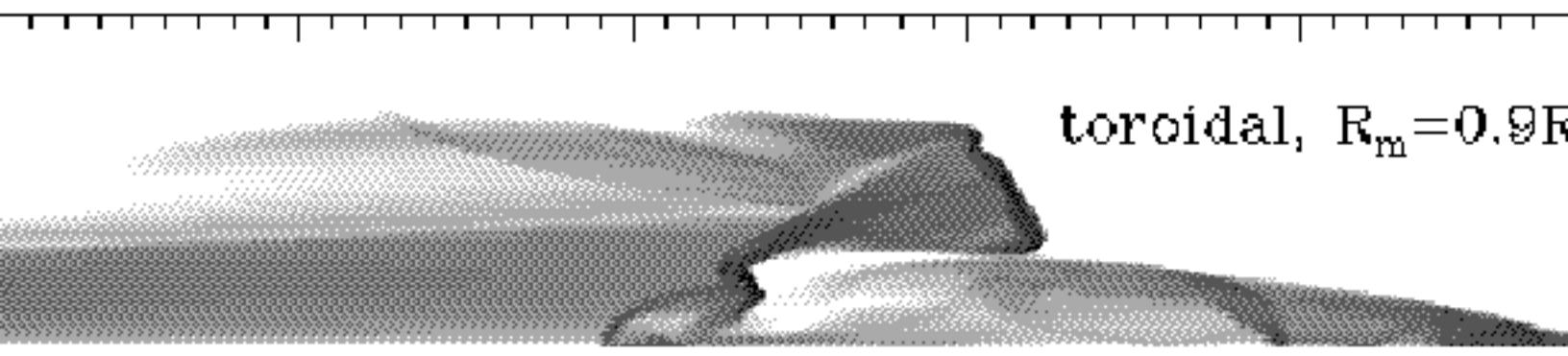
 z/R_j











60 70 80 90

z/R_j

